

# Numerical estimation and application of slamming wave impact on monopile structures

Master thesis

Sicco Dommerholt





# Numerical estimation and application of slamming wave impact on monopile structures

## Master thesis

by

Sicco Dommerholt

Student:	Sicco Dommerholt	
Thesis committee:	Prof. dr. A. V. Metrikine,	TU Delft
	Dr. ir. M. Zijlema,	TU Delft
	Ir. T. C. Raaijmakers,	TU Delft
	Ir. K. Hermans,	ECN





# Preface

This master thesis was conducted at the Delft University of Technology in order to obtain the master of science degree of the master Offshore and Dredging Engineering. The research has been executed at Energieonderzoek Centrum Nederland (ECN) within the Wind Energy department.

Herewith, I would like to kindly thank especially Koen Hermans from ECN for his support throughout the graduation process. Also I want to kindly thank my committee and all those who supported me during my graduation.

Writing my thesis was a valuable process from which I have learned the many different aspects of the subject and the research process.

*Sicco Dommerholt*



# Summary

For the offshore wind industry it is essential to further reduce costs to be competitive to traditional energy resources. One of the options to achieve so is optimizing support structure design. Using XL-monopiles allows for larger turbines, deeper water access and consequently can provide for a more cost effective support structure. Within this market, Energieonderzoek Centrum Nederland (ECN) operates with its in-house developed software package to evaluate turbine responses. To further improve the model, a better insight is needed in breaking wave impacts on structures.

This thesis is focused on developing an enhanced method to evaluate breaking waves on monopile structures to identify the effect of slamming waves on XL-monopiles. Based on wave tank measurements, a method to identify slamming wave impacts is developed and tested. Later, those wave tank measurements are reproduced and the identification method verified.

Wave tank experiments were carried out at the Atlantic Basin at Deltares within the joint industry research project WiFi. For the experiments, two monopile scale models were placed in the wave tank, both equipped with multiple load and pressure sensors. During the tests the monopiles were exposed to series of wave trains, the irregular wave trains with a total of approximately 5000 waves, created a large sample size needed for the experiment. The wave measurements from the tank are analysed numerically to identify breaking waves. In this thesis a slamming wave event definition is proposed as follows:

- Front crest steepness  $S$  should reach breaking limit
- The slamming impact of the wave should be more than 4 times the standard deviation of the force time series

The numerical computations are carried out using the potential flow solver OceanWave3D to generate a sea state with comparable characteristics to the wave tank measurements. At first, the generated sea state appeared to lack the necessary wave height. By adjusting the input in the OceanWave3D program, a sea state was found that matches the measurements. Wave energy dissipation is checked throughout the measurements wave tank and compared to dissipation in the numerical model. It was shown that both the wave tank and numerical model show resembling dissipation.

Hydrodynamic loading on the monopile foundation is assessed using the kinematics obtained from the OceanWave3D model. Several methods were combined to come to the total wave loading. First the Morison approach was used to account for the non-slamming part for the wave load. Using OceanWave3D, the force coefficients are

calculated applying DNV guidelines. The second part, the slamming part of the wave load, is obtained in multiple phases. First, based on the above mentioned slamming wave criteria, wave steepness and impact forces, the individual waves are evaluated and scored as potential slamming. Secondly, using conservation of momentum and kinematics derived from OceanWave3D, the slam load is calculated. This slam load is determined evaluating the impact velocity of all waves individually and added to the Morison load if identified as slamming. Finally, when the calculated impact loads from the numerical model are compared to the recorded loads in the wave tank measurements, large similarity can be noticed.

After comparison of the developed slam load representation to the DNV method of slam load estimation, the result is a less conservative slam load approximation. This is due to the evaluation of slamming impact velocities per wave, opposed to the assumption of a single impact velocity for the whole sea state. The results of this thesis can further implemented in turbine response evaluation tools by ECN resulting in a more optimized calculation model. It will enable the design of more (cost)efficient XL-monopile structures.



# Contents

<b>1</b>	<b>Introduction</b>	<b>1</b>
1.1	Background . . . . .	1
1.2	Problem statement . . . . .	1
1.3	Approach . . . . .	2
1.4	Thesis outline . . . . .	3
<b>2</b>	<b>Wave theory</b>	<b>5</b>
2.1	Free surface waves . . . . .	5
2.1.1	Potential flow . . . . .	7
2.1.2	Linear wave theory . . . . .	8
2.1.3	Stokes non-linear waves . . . . .	9
2.1.4	Stream function waves . . . . .	10
2.1.5	Breaking waves . . . . .	11
2.2	Wave loads on cylinders . . . . .	13
2.3	Slamming wave loads . . . . .	14
2.3.1	Derivation slam load . . . . .	14
2.3.2	Implementation of slam load formulation . . . . .	17
2.4	OceanWave3D . . . . .	19
2.5	Wave analysis . . . . .	21
<b>3</b>	<b>Measurement data</b>	<b>25</b>
3.1	Experimental set-up . . . . .	25
3.2	Data selection . . . . .	27
3.2.1	Identification of slamming waves . . . . .	28

3.2.2	Identification of slamming waves ECN . . . . .	30
3.3	Processing . . . . .	30
3.4	Summary . . . . .	31
<b>4</b>	<b>Numerical wave modelling</b>	<b>33</b>
4.1	Set-up numerical wave tank . . . . .	33
4.2	Validate numerical wave tank . . . . .	34
4.3	Select input sea state . . . . .	36
4.4	Long numerical model. . . . .	39
4.5	Summary . . . . .	40
<b>5</b>	<b>Impact loading in numerical model</b>	<b>41</b>
5.1	Wave loading on monopile. . . . .	41
5.1.1	Force coefficients . . . . .	42
5.1.2	Wave loading . . . . .	43
5.2	Identify potential slam waves . . . . .	44
5.3	Slamming wave load. . . . .	45
5.3.1	Slam coefficient . . . . .	46
5.3.2	Impact velocity. . . . .	47
5.3.3	Numerical slam load results . . . . .	47
5.4	Summary . . . . .	50
<b>6</b>	<b>Conclusions and recommendations</b>	<b>51</b>
6.1	Conclusions . . . . .	51
6.2	Future work . . . . .	52
<b>A</b>	<b>Measurement data plots</b>	<b>53</b>
A.1	Time series. . . . .	53
A.2	Individual waves . . . . .	55

<b>B OceanWave3D data plots</b>	<b>57</b>
B.1 Time series. . . . .	57
B.2 Individual wave plots. . . . .	57
<b>C OceanWave3D input</b>	<b>59</b>
<b>Bibliography</b>	<b>61</b>



# 1

## Introduction

### 1.1. Background

Global awareness of human induced climate change is rising. Governments and corporations are investing more resources in the development of renewable energy sources. Today, renewable energy represents only a small percentage of the total power production. Within the 2015 Paris Agreements, many countries acknowledged the complications of future climate change and agreed on reducing carbon emissions 40 % by 2030 [7]. Prior to the Paris climate summit, the Dutch government signed agreements in 2013 moving towards a more sustainable future. The goal was set that by 2020, 14 % [19] of the total energy consumption has to be generated by renewable resources. This is planned to grow to 16 % in 2023. In pursuance of these goals, the Dutch government aims to increase the national offshore wind energy production by 3450 MW in 2023, a boost of 345 % [19] compared to 2013. To safeguard the future of offshore wind, it needs to be made more competitive compared to traditional fossil fuel resources. Therefore, a large cost-reduction needs to be realised. From this perspective it is essential to have maximisation of the yield and cost effectiveness. Generally, a solution to achieve so, is to up-scale the wind turbines. Larger turbines can generate more power output with the same amount of installed monopiles. While many want clean and sustainable energy, the principle of not-in-my-back-yard prevails. Consequently, the trend pushes the wind farms further offshore, where turbines are constructed in deeper waters.

### 1.2. Problem statement

As mentioned earlier, the so called XL-monopiles are placed far offshore, preferably on relatively shallow waters. On the banks, waves and swell come from deeper waters and rapidly enter shallow waters. The inclination of the seabed can result in the waves to break at the bank [10]. Slamming of waves on the monopile can create tremendously high loads, with added slam peak loads of 60 % [17]. The effects of

such high loading on thin-walled monopiles are yet uncertain under and modelling is required to gain insight. To be able to properly assess the loading, a more in depth insight is required for breaking waves. Therefore, this thesis will focus on analysing the effect of breaking waves on XL-monopiles. From here, the following main research objective for this thesis is derived:

Establish an enhanced breaking wave model to identify the effect of slamming waves on XL-monopiles.

ECN uses its in-house software package Phatas to calculate environmental loads on wind turbines. The computer program Phatas, "Program for Horizontal Axis wind Turbine Analysis and Simulation", is developed for the time-domain calculation of the dynamic behaviour and the corresponding loads on a horizontal axis wind Turbine. Phatas is available as tool in the integrated wind turbine design package FOCUS6. The program Phatas is in particular capable for the analysis of offshore turbines, by having an improved model for tower dynamics which allows wind and wave loading and motions of the tower base.

Opposed to the industry standard, where an embedded stream function defines a single wave loading, ECN uses potential flow solver OceanWave3D to generate a sea state with multiple steep waves. The individual waves are evaluated and potential slamming impacts are selected and used for calculation of impact forces on the monopile. Subsequently, the slamming force is added as a rectangular impulse to monopile.

It is unclear whether the method used by ECN suffices in accuracy, where overestimating the slam load could be the case. The potential flow solver OceanWave3D predicts high particle velocities, resulting in high slam loads. This way, the slam load will be accounted for two times ending up with overestimation.

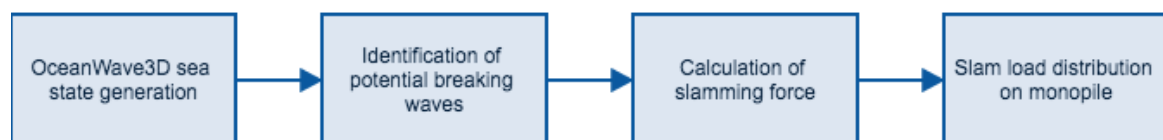


Figure 1.1: Current calculation steps to determine slam load used by ECN.

### 1.3. Approach

The currently used method by ECN to evaluate slam load on monopiles, serves simplicity but unfortunately lacks accuracy. The goal for this thesis is to enhance breaking wave load estimates on XL-monopiles for ECNs in-house software PHATAS. To be able to achieve this, the research is subdivided into the following sub-objectives:

- Analyse breaking wave conditions

- Analyse breaking wave loads acting on monopile
- Analyse different methods to represent slam load

Using wave measurement data from wave tank tests performed for the joint industry research project WiFi at the Atlantic basin with Deltares, slam load representation is compared. The enhanced breaking wave model can later be used to be implemented in ECNs in-house software Phatas.

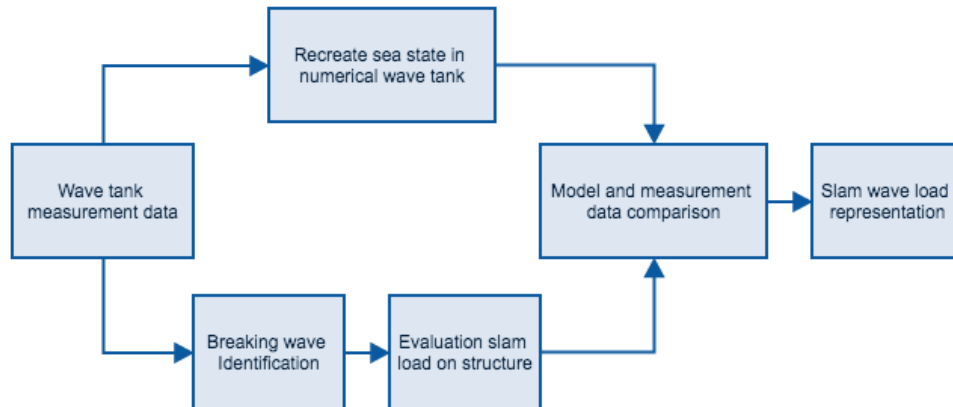


Figure 1.2: Approach for thesis with steps to be undertaken.

## 1.4. Thesis outline

The thesis is structured as follows. After the general introduction and outline of the problem in this chapter, Chapter 2 follows with a review of the applicable wave theories for this thesis. Furthermore, load calculation methods are proposed. Additionally, the potential flow solver OceanWave3D is introduced, along with its working principles. Continuing with Chapter 3, the measurement data from the WiFi experiments are analysed and presented. Moreover, here is the identification of the breaking wave introduced. In Chapter 4 simulations performed in OceanWave3D are presented in tables and graphs. The measurement data and simulations from OceanWave3D are then compared and analysed in Chapter 5. Here, slam load calculations are done and various representations are considered. Finally, the thesis concludes with suggested recommendations.





# 2

## Wave theory

Typically, when looking in wave loading on offshore structures, engineers are firstly interested in kinematics of the waves. To gain better insight in the complexity of breaking waves, the wave theory in this chapter is broken down in segments. Initially, the basics of wave generation are reviewed. Further on, breaking waves and wave loading are addressed. Getting more close to the actual research objective, industry practices are described and further explained.

### **2.1. Free surface waves**

Looking at the ocean shows us a wide variety of waves. Numerous individual crest heights and different wave periods can be observed. Throughout this section the origin of different types of ocean waves are discussed. Depicted in figure 2.1 is the spectrum of the different types of ocean waves. For this thesis we are mainly interested in waves with a period of 10s and smaller. Hence, we focus on swell, wind waves and capillary waves. These waves are generated by wind interaction on the water surface. The smallest of the three, capillary waves, can be seen as small wrinkles and generally cause only some sea spray. Due to their small energy level capillary waves will be neglected in this research.

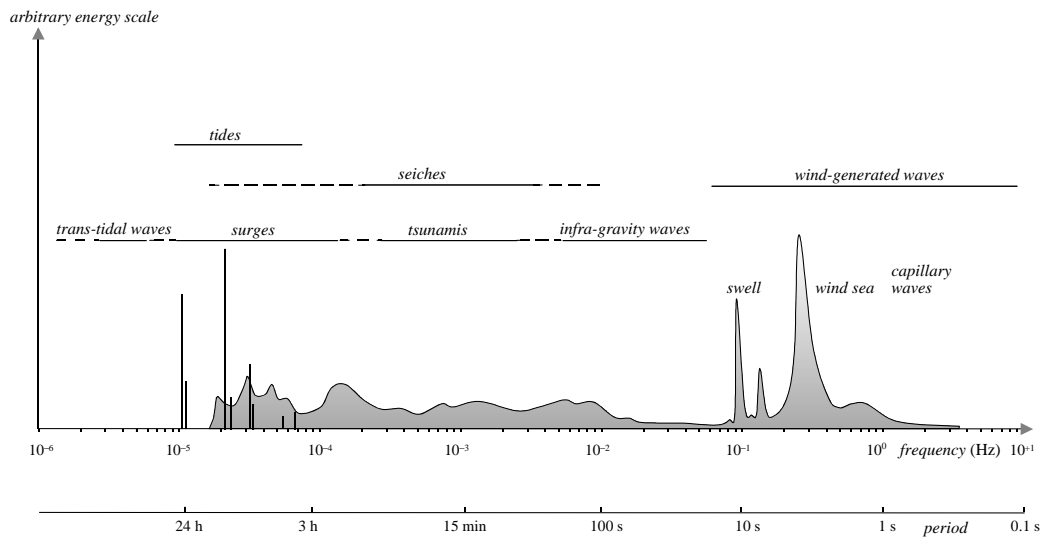


Figure 2.1: Frequencies and periods of the vertical motions of the ocean surface [10].

As mentioned in the previous paragraph, wind waves are caused by wind interaction on the ocean surface. Figure 2.2 shows three different stages of wind wave generation. Initially, friction between air and water will cause the generation of small wrinkles on the ocean surface. Once more energy is transferred from the wind to the water, the small wrinkles will start to evolve into substantial crests. The process of wave generation can continue until wind and wave have equal velocity, or until the wave reaches maximum wave height. The so-called breaking limit marks the maximum crest height of a wave in certain conditions. When the breaking condition is met, wave breaking will occur.

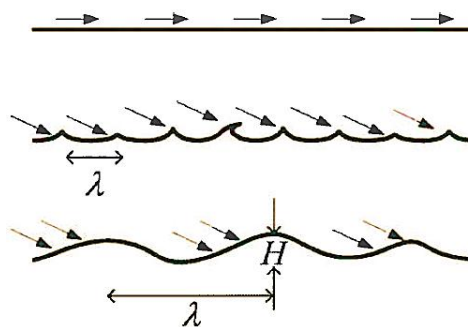


Figure 2.2: Development of wind generated waves. As wind interact with the ocean surface, waves grow to certain waveheight and wavelength [10].

The validity of different wave theories have been intensely researched and the results of several studies are depicted in figure 2.3. Later in this chapter these theories are further elaborated on. The picture shows the applicability of the theories to certain wave conditions. Other wave theories are discussed in upcoming sections. As can be seen in figure 2.3, the theories, both linear and non-linear, are only valid up-to the breaking limit  $H_b$ . In the upcoming paragraphs the different wave theories are further analysed.

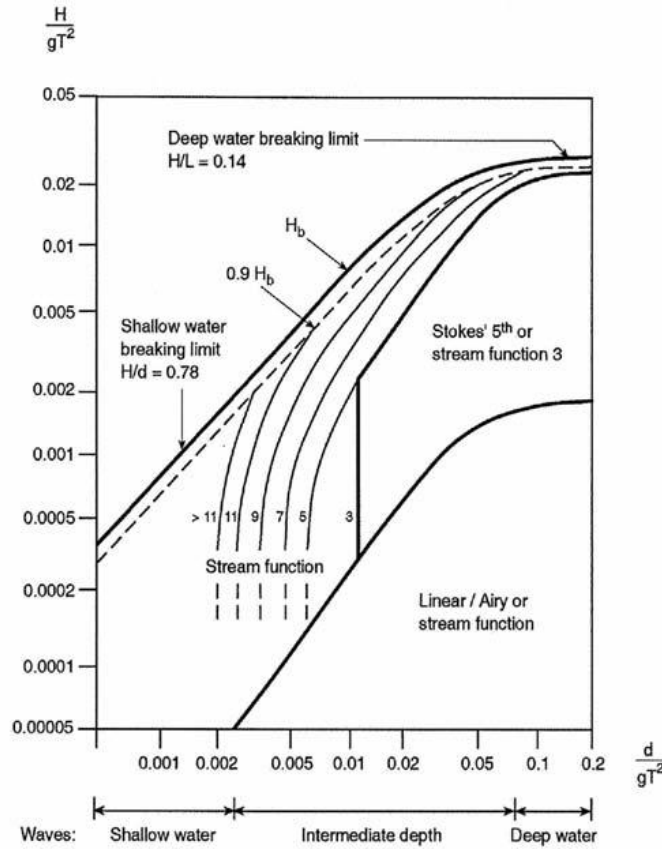


Figure 2.3: The ranges of applicability of various wave theories and their range of applicability[5] .

### 2.1.1. Potential flow

Potential flow can be used to describe the velocity potential in a fluid. The velocity potential function  $\phi$  is based on conservation of mass and momentum where the fluid is assumed to be irrotational, incompressible and inviscid.

The particle velocities can be expressed as functions of space and time:

$$u = \frac{\partial \phi}{\partial x}, \quad v = \frac{\partial \phi}{\partial y} \quad \text{and} \quad w = \frac{\partial \phi}{\partial z} \tag{2.1}$$

The conservation of mass results in the continuity equation:

$$\frac{\partial u}{\partial x} + \frac{\partial v}{\partial y} + \frac{\partial w}{\partial z} = 0 \tag{2.2}$$

The continuity equation expressed in terms of the velocity potential:

$$\nabla^2 \phi = \frac{\partial^2 \phi}{\partial x^2} + \frac{\partial^2 \phi}{\partial y^2} + \frac{\partial^2 \phi}{\partial z^2} = 0 \tag{2.3}$$

Equation 2.3 is called the Laplace equation.

Now the continuity equation is expressed in terms of  $\phi$ , the Momentum balance is to be derived. Momentum balance for a fluid in z-direction is found as:

$$\frac{\partial w}{\partial t} + \frac{\partial(uw)}{\partial x} + \frac{\partial(vw)}{\partial y} + \frac{\partial(ww)}{\partial z} = -\frac{1}{\rho} \frac{\partial p}{\partial z} - g \quad (2.4)$$

Differentiation using chain rule gives us the following equation of motion:

$$\frac{\partial w}{\partial t} + \frac{\partial}{\partial z} \left( \frac{1}{2}u^2 + \frac{1}{2}v^2 + \frac{1}{2}w^2 \right) = -\frac{1}{\rho} \frac{\partial p}{\partial z} - g \quad (2.5)$$

After changing the order of differentiation in the equation of motion in 2.5, a constant term for motions in x-,y- and z- direction is found. This constant term forms the Bernoulli equation:

$$\frac{\partial \phi}{\partial t} + \frac{1}{2} \left[ \left( \frac{\partial \phi}{\partial x} \right)^2 + \left( \frac{\partial \phi}{\partial y} \right)^2 + \left( \frac{\partial \phi}{\partial z} \right)^2 \right] + \frac{p}{\rho} + gz = 0 \quad (2.6)$$

Equation 2.6 represents the Bernoulli equation for unsteady motion and in vector notation takes the following form:

$$\frac{\partial \phi}{\partial t} + \frac{1}{2} |\nabla \phi|^2 + \frac{p}{\rho} + gz = 0 \quad (2.7)$$

The equations explained above form the basis for wave modelling theories. In further sections different interpretations are evaluated.

### 2.1.2. Linear wave theory

Regular ocean waves travelling in deep water can be characterised by linear wave theory, often referred to as Airy wave theory. Airy wave theory gives a linearised description of wave propagation on the free surface. It can be applied in sea state modelling and describes the wave kinematics. Linear waves are based on potential flow on a mass balance equation and momentum balance equation[10] and when both are expressed as the velocity potential function  $\phi$ , it results in a Laplace and Bernoulli equation respectively.

Filling out the kinematic boundary conditions at the surface and the bottom for the Laplace equation in 2.3 the kinematic boundary conditions result in:

$$\frac{\partial \phi}{\partial z} = \frac{\partial \eta}{\partial t} \quad \text{at } z = 0 \quad (2.8)$$

And for the kinematic boundary condition at the seabed:

$$\frac{\partial \phi}{\partial z} = 0 \quad \text{at } z = -d \quad (2.9)$$

As stated before, the momentum balance equations in 2.4 describe the Bernoulli equation and can be written in linearised form:

$$\frac{\partial \phi}{\partial t} + \frac{p}{\rho} + gz = 0 \quad (2.10)$$

The dynamic boundary conditions expressed in terms of the velocity potential:

$$\frac{\partial \phi}{\partial t} + g\eta = 0 \quad \text{at } z = 0 \quad (2.11)$$

Using the kinematic boundary conditions from 2.8, a solution for the Laplace equation in 2.8 describes a harmonic propagating wave and its wave elevation:

$$\eta(x, t) = a \cos(\omega t - kx) \quad (2.12)$$

where,  $a$  represents the wave amplitude,  $\omega$  wave angular frequency and  $k$  the wave number. This linear propagating wave is only valid for small amplitudes compared to wavelength and water depth.

### 2.1.3. Stokes non-linear waves

When water becomes too shallow and waves become steeper, linear wave theory will not apply anymore. As can be noted in figure 2.4, real waves differentiate in form from the earlier described cosine waves. A better approximation of the wave is found by correcting the cosine wave profile. With correction factors in Stokes theory, the wave profile is adjusted to be steeper and better fit the real wave profile. Stokes theory uses the wave steepness  $\epsilon = ak$  to describe the basic harmonics, so the harmonics for a first order linear wave are written as:

$$\eta(x, t) = a \cos(\omega t - kx) = \epsilon \eta_1(x, t) \quad (2.13)$$

A second order Stokes non-linear wave is then given as:

$$\eta(x, t) = \epsilon \eta_1(x, t) + \epsilon^2 \eta_2(x, t) \quad (2.14)$$

Which can also be described as follows:

$$\eta(x, t) = a \cos(\omega t - kx) + ka^2 \frac{\cosh(kd)}{4 \sinh^3(kd)} [2 + \cosh(2kd)] \cos[2(\omega t - kx)] \quad (2.15)$$

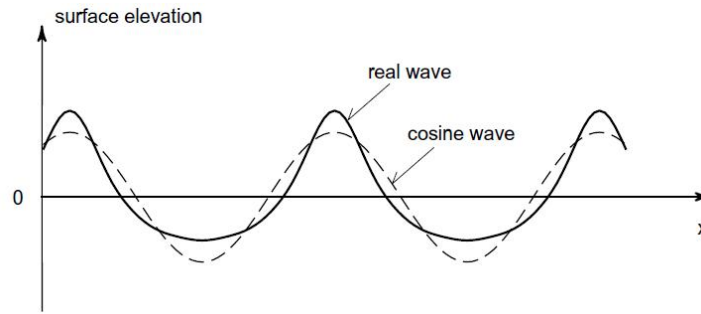


Figure 2.4: Linear cosine waves plotted with representation of a real wave [10].

Here the first term on the right-hand side represents the Airy wave and the left-hand side forms the second-order Stokes correction. This second order Stokes wave is symmetrical around the crest (horizontally) and vertically asymmetrical. In the equation is a second harmonic added to form the second-order Stokes equation. It can be noted in figure 2.5 that the Stokes wave has a sharper crest and slightly flatter trough.

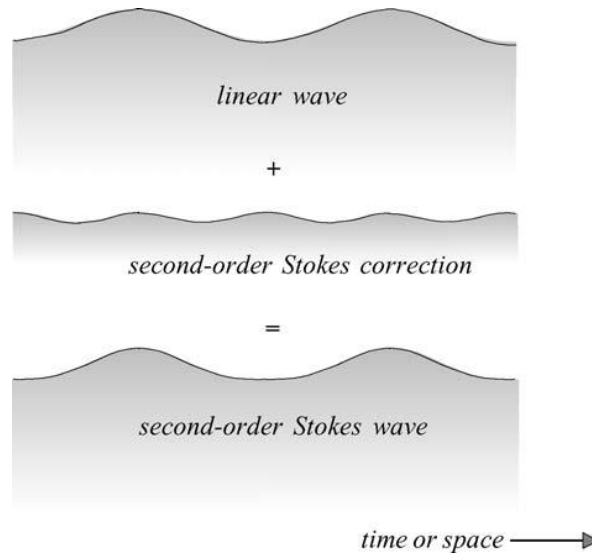


Figure 2.5: Surface representation second-order Stokes wave [10].

Continuing with the Stokes equation presented in equation 2.15, more harmonics can be added. Adding more harmonics enhances the approximation of the Stokes equation; This will result in the following representation:

$$\eta(x, t) = \varepsilon\eta_1(x, t) + \varepsilon^2\eta_2(x, t) + \varepsilon^3\eta_3(x, t) + \varepsilon^4\eta_4(x, t) + \dots \quad (2.16)$$

#### 2.1.4. Stream function waves

Another commonly used approximation of the wave profile is found by Dean[4] in his stream function theory. Unlike the previous theories, the equations are not solved using the velocity potential  $\phi$ , but rather using the stream function  $\psi$ .

$$\frac{\partial \psi}{\partial z} = u \quad \left( = \frac{\partial \phi}{\partial x} \right) \quad (2.17)$$

$$-\frac{\partial \psi}{\partial x} = w \quad \left( = \frac{\partial \phi}{\partial z} \right) \quad (2.18)$$

Here, multiple higher order harmonic waves are added simultaneously which will fit the dynamic boundary conditions perfectly. In the stream function the 2-D continuity of the water mass is always guaranteed:

$$\frac{\partial u}{\partial x} + \frac{\partial w}{\partial z} = \frac{\partial^2 \psi}{\partial z \partial x} - \frac{\partial^2 \psi}{\partial x \partial z} = 0 \quad (2.19)$$

Equation 2.20 shows a solution of the stream function in general form, where  $c$  is wave celerity and  $N$  is the order of the wave theory. For instance, when  $N = 1$ , the stream function theory reproduces the linear wave theory.

$$\psi(x, y) = cz + \sum_{n=1}^N X(n) \sinh nk(z + d) \cos nkx \quad (2.20)$$

Both the wave theories of Dean and Stokes have limitations. Stream function waves are applicable in shallow waters, whereas Stokes waves are suited for deep water ocean waves. The validity and the ranges of the various wave theories are depicted in figure 2.3.

The stream function describes the steep waves well, even for waves close to the breaking limit. The closer to breaking limit of the wave, the more order terms  $N$  have to be added to have an accurate representation of the wave. Since a stream function needs predefined input parameters such as wave height, peak period and water depth, it is predominantly used to estimate extreme loads. To resemble a larger sea state, the stream function wave is not ideal and therefore other theories are more suited.

### 2.1.5. Breaking waves

Free surface waves are limited in height. When the maximum height is reached, the wave will break and energy is dissipated from the wave. Over the years research is done on the actual conditions of the free surface waves in which waves will tend to break.

Longuet-Higgins [12] proposed a breaking wave criterion based on the gravitational acceleration. According to Higgins, when the downward acceleration of a wave exceeds  $0.5g$ , the wave will break. This rather simple criterion is still used as a first estimate for breaking waves. Further investigations were done by Williams [22] on

limited amplitude waves. Where previous methods use a form of series expansion which use many terms to describe the wave form accurately, Williams introduced a specific crest term based on water depth and waves steepness. This drastically increased the practical implementation.

As waves travel to more shallow waters, they become steeper. The height of depth induced breaking waves is limited and collapsing occurs near the wave breaking limit. Generally, four types of wave breaking can be recognised [9]; spilling breaker, plunging breaker, collapsing breaker and surging breaker.

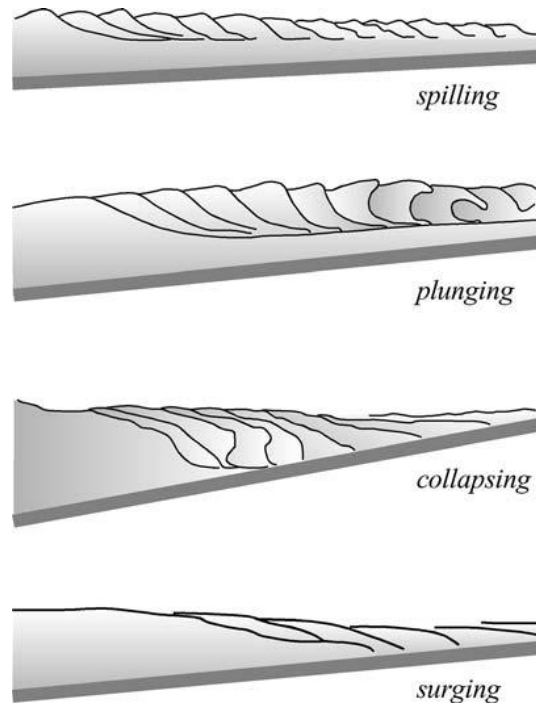


Figure 2.6: The four main types of breaking waves [10]. a) spilling, b) plunging, c) collapsing, d) surging waves.

To what type of breaker the wave is assigned, is dependant on a dimensionless parameter, the Iribarren number [1]. The Iribarren number shows the relation between the sloping bed ratio and the wave steepness.

$$\xi_b = \frac{m}{\sqrt{\frac{H_b}{\lambda_0}}} \quad (2.21)$$

where  $H_b$  is the wave height at breaking,  $m$  is the slope of the beach and  $\lambda_0$  is the deep water wavelength. Based on equation 2.21, the breaking waves are qualified as follows:

- Spilling - White water at the top of the crest and water will spill down at the front of the wave.  $\xi_b < 0.4$



- Plunging - Front face steepens until crest curls over the front face.  $0.4 < \xi_b < 2$
- Collapsing - A combination of plunging and surging. Front face curls over as short plunging breaker with splash-up.  $\xi_b \approx 2$
- Surging - When wave runs up a steep beach, foam forms at beach surface.  $\xi_b > 2$

The peak force due to a breaking wave highly depends on the breaker type. The peak force is significantly increased for a plunging breaking wave [3].

## 2.2. Wave loads on cylinders

Compared to wind and current loading, waves form the majority of the load undergone by an offshore monopile. This high contribution in environmental loading underlines the importance of a proper model for wave load calculation.

A cylinder is considered to be slender when the diameter of the structure is much smaller than the wavelength of the incoming wave. For offshore monopiles this is the case.

The wave forces acting on an monopile are the result of inertia and drag forces. Based on Potential flow theory, the inertia force on a monopile can be deducted. In the inertia force, the drag of the structure is neglected. The drag force is as found when you have steady flow on a structure and is proportional to  $u^2$  and the cylinder diameter [11].

Based on the above, to be able to estimate the loads on a vertical cylinder, Morison [14] superimposed the linear inertia force and the quadratic drag force to calculate the force acting on the structure.

$$F(t) = F_{inertia}(t) + F_{drag}(t) \quad (2.22)$$

Which can also be expressed as follows:

$$F_m(t) = C_m \rho \frac{\pi}{4} D^2 \dot{u}(t) + C_d \frac{1}{2} \rho D u(t) |u(t)| \quad (2.23)$$

where  $C_m$  and  $C_d$  are empirical coefficients for inertia and drag respectively,  $\dot{u}(t)$  water particle acceleration and  $u(t)$  the water particle velocity.

The inertia and drag components in equation 2.23 are 90° out of phase, this is due to the phase shift between velocity and acceleration. The phase shift is shown in figure 2.7.

$C_m$  and  $C_d$  are empirical coefficients and can be determined in several ways [11] and typical suggested values are given by design codes. Values for  $C_m$  range from 1.5 to 2.0 and values for  $C_d$  from 0.6 to 1.6. Important parameters to determine the right values are the Keulegan Carpenter number (KC) and the Reynolds number.

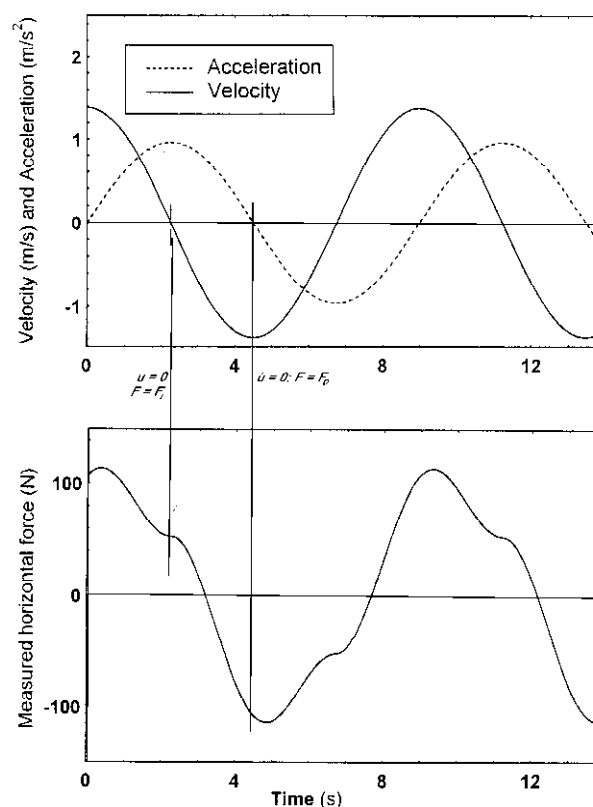


Figure 2.7: Phase shift between acceleration and velocity and the relation to total horizontal hydrodynamic force [11].

## 2.3. Slamming wave loads

In this section the wave loading of breaking waves on the monopile is discussed. Firstly, a method to represent the breaking wave impact is derived. Secondly, the practical implementation for the derived method is addressed.

### 2.3.1. Derivation slam load

The hydrodynamic force on a cylinder can be parted in a slamming and a quasi-static component. Slamming can occur when a breaking wave hits the structure. The slamming impact results in high impulse loading on structures. The quasi static and slam load are both of comparable magnitude, as shown in figure 2.8. This shows the significance of the the slamming force on the monopile. Although of comparable magnitude, impact times will differ. Hence the slamming part, with short impact time, will mainly govern the dynamic response of tower. Whereas the the non-breaking part of the wave, has most effect on the global response [17].

For years, the industry has used Morison's theory to evaluate quasi-static hydrodynamic loading on cylindrical structures. But as stated previously, for a breaking wave the total wave impact consists of both the quasi-static and slamming part. Therefore,

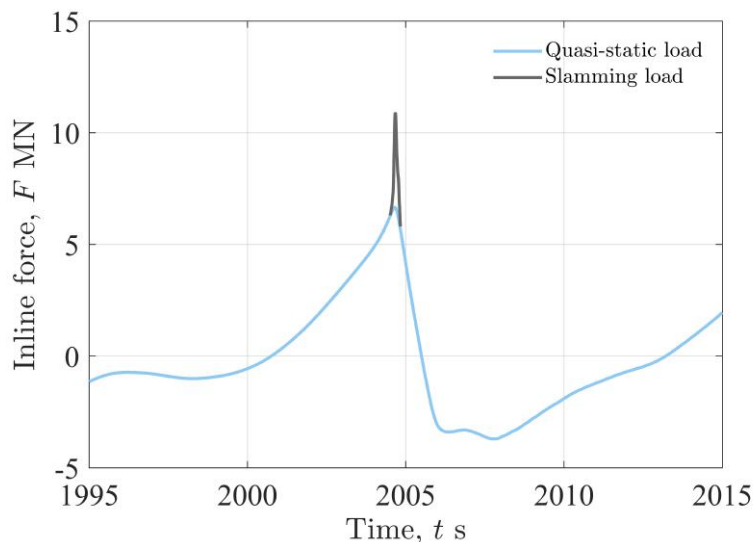


Figure 2.8: Measured base shear from breaking wave impact, with contribution of slam load in black [17]

an additional term is added to compute the total wave force on the structure:

$$F = F_{inertia} + F_{drag} + F_{slam} \quad (2.24)$$

This new term,  $F_{slam}$ , is the slam force which is super imposed to form the total wave force. A theoretical approach to slamming wave impact can be defined following Sarpkaya [18]; considering a fixed and rigid monopile, which is vertically subdivided in strips  $dz$ , is located in a control volume of mass  $M$ . The control volume has horizontal velocity  $u_0$ . The mass of the water has a horizontal momentum of  $p = Mu_0$ . It is assumed that the total horizontal momentum remains constant during impact. After the breaking wave impact, due to the fluid motion around the structure, an added mass term  $m_a$  is introduced. Since the momentum before and after impact is constant,  $u_0$  is reduced to a new velocity  $u$ .

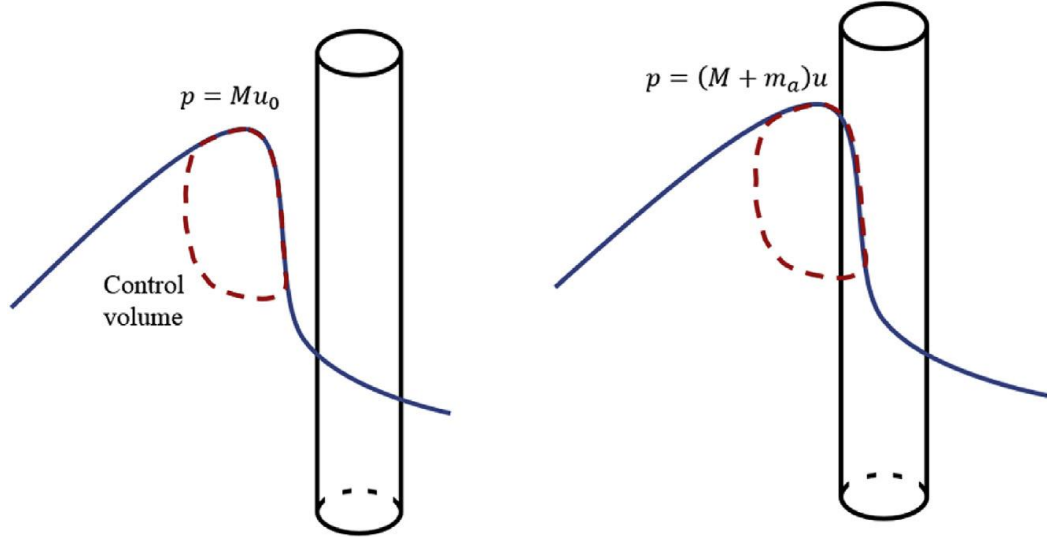


Figure 2.9: Breaking wave on cylinder before(left) and after(right) impact [20].

$$p = Mu_0 = (M + m_a)u \quad (2.25)$$

Using Newton's second law, the horizontal force on the pile is calculated:

$$dF = \frac{dp}{dt} dz = \left( (m_a + M) \frac{du}{dt} + u \frac{dm_a}{dt} \right) dz \quad (2.26)$$

First term in equation 2.26 is the added mass load on the structure. Second term is the slam load  $dF_{slam}$  and uses the time varying added mass [8]. Since we are only interested in the slam force on the monopile we focus on the latter part of the equation:

$$dF_{slam} = u \frac{dm_a}{dt} dz \quad (2.27)$$

where  $u$  is the horizontal wave particle velocity at the free surface and  $\frac{dm_a}{dt}$  represents the rate of change of the added mass during a slamming impact.  $m_a$  is given for a fixed smooth cylinder as [5]:

$$m_a = C_a \rho A_i \quad (2.28)$$

with  $C_a$  the added mass coefficient and is for a vertical smooth cylinder equal to 1,  $\rho$  the density of water and  $A_i$  the slam impact area per unit length.

When the the momentum change is evaluated for a small time duration from just before impact to right after, duration  $dt$  is  $\frac{dx}{u}$ . Hence the change of added mass can be written as follows:

$$\frac{dm_a}{dt} = (C_a \rho A_i) \frac{d}{dt} = C_a \rho u \frac{A_i}{dx} \quad (2.29)$$

Combining equations 2.27 and 2.29 will result in the slam force acting on the structure per unit length and dependent on the varying added mass  $\frac{A_i}{dx}$ :

$$dF_{slam} = C_a \rho u^2 \frac{A_i}{dx} dz \quad (2.30)$$

$\frac{A_i}{dx}$  can be expressed by a slamming coefficient  $C_s$ .  $C_s = \frac{2}{\rho D} \frac{A_i}{dx}$  and is derived analytically in several studies.  $C_s$  will be analysed further in this thesis. Implementing the new slam coefficient in equation 2.30 will result in the following:

$$dF_{slam} = \frac{1}{2} \rho C_s D u^2 dz \quad (2.31)$$

Integrating over the height of the impact area, gives a general slam impact load on the monopile.

$$F_{slam} = \int dF = \frac{1}{2} \rho C_s A u^2 \quad (2.32)$$

### 2.3.2. Implementation of slam load formulation

Once the slamming wave load on the monopile is theoretically derived in the previous section, a more general formulation of the slam load is presented in the upcoming part. Several interpretations of the slam load and its input parameters are given.

Following the DNV guidelines the slam force is calculated as follows [5]:

$$F_{slam} = \frac{1}{2} \rho_w C_s A u^2 \quad (2.33)$$

where  $\rho_w$  is water density,  $u$  is the water particle speed,  $C_s$  represents the slamming coefficient and for a smooth cylinder can be taken as  $2\pi$  and  $A$  the impact area of the incoming slam wave.

The particle velocity  $u$  of an incoming wave on the structure in equation 5.9, should be calculated as follows:

$$u = 1.1c = 1.1 \frac{\lambda}{T_b} \quad (2.34)$$

where  $c$  is phase velocity,  $\lambda$  wavelength and  $T_b = 0.9T_p$

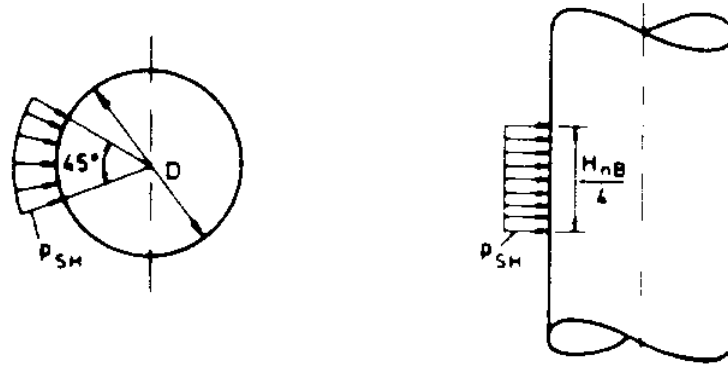


Figure 2.10: Definition of impact area of slamming wave on cylinder based on DNV-RP-C205 code. [5].

As shown in figure 2.10, the impact area of the slamming wave is defined as  $45^\circ$  of the cylinder. The height of the breaking impact area is based on the height of the breaking wave,  $H_b$ , and set to  $0.25H_b$ . The breaking wave height, may be taken as 1.4 times the significant wave height [5].

$$A = \frac{1}{32}H_b D \pi \quad (2.35)$$

The duration of the slamming impact on the cylinder is determined by Wienke [21] and for a plunging wave that breaks directly in front of the monopile, the duration of the impact can be taken as follows:

$$t_{impact} = \frac{13D}{64c} \quad (2.36)$$

where  $D$  is the diameter of the monopile and  $c$  the phase velocity of the wave.

Apart from the slam load representation from DNV, more recent study by Paulsen et al. describes the  $F_{slam}$  as follows [17]:

$$F_{slam} = \frac{1}{2}\rho_w u^2 C_s f(t) \lambda H_b D g(z, y) \quad (2.37)$$

where  $\rho$  water density,  $u$  impact velocity,  $C_s$  a slam coefficient,  $f(t)$  temporal development of impact,  $\lambda$  the curling factor which indicates the height of the impact area regarding to the incoming wave,  $H_b$  the wave height just before breaking,  $D$  pile diameter and  $g(z, y)$  represents the spatial distribution of the slam load on the monopile.

Having multiple unknowns in equation 2.37, it is needed to evaluate these further. The shallow water approximation for wave celerity is observed to be sufficiently accurate

[17], hence  $u = \sqrt{gh}$ . Slam coefficient  $C_s$  represents the added mass coefficient for a cylinder and thus has the value  $C_s = 2\pi$ .

The temporal development in equation 2.37 is a little more elaborate to characterise. Within the studie it is found that  $f(t)$  is best represented by a harmonic function:

$$\sin^2\left(\pi\frac{t}{T_{impact}}\right) \quad (2.38)$$

This means that the slam load follows the harmonic  $\sin^2$  function for a period of  $T_{impact}$ . The impact duration is chosen to be  $13D/32u$ .

Based on the experimental data curling factor of the slamming wave is assessed and the following estimate can be used:

$$\lambda = 0.29\frac{H_b}{H_s} \quad (2.39)$$

Finally, the integrated slam load on the monopile is given by:

$$F_{slam}(t) = \frac{1}{2}\rho_w(\sqrt{gh})^2 2\pi \sin^2\left(\pi\frac{t}{T_{impact}}\right) \lambda H_b D \frac{2}{\pi^2} \quad (2.40)$$

It can be seen that equations 5.9, 2.33 and 2.40 are closely related and share the same theoretical background. Summarised in table ?? are the parameters for the different slam load notations. Later in this thesis the appropriate parameters are selected and implemented in the slam load calculation.

	slamming coefficient $C_s$ [-]	impact area $A$ [ $m^2$ ]	impact time $T_i$ [s]	impact velocity $u$ [ $\frac{m}{s}$ ]
DNV	$2\pi$	$\frac{1}{32}H_b D \pi$	$\frac{13D}{64c}$	$1.1\frac{\lambda}{T_b}$
Paulsen et al.	$2\pi$	$\lambda H_b D \frac{2}{\pi^2}$	$\frac{13D}{32c}$	$\sqrt{gh}$

Table 2.1: Input parameters for different slam formulations.

## 2.4. OceanWave3D

The fully non-linear potential flow solver OceanWave3D (OCW3D) can be used to generate numerical sea states. The numerical solver describes propagation and development of fully nonlinear waves up to the breaking height. The OceanWave3D software is developed by Ensig-Karup and Bingham [6]. In this section the working principles of the solver are discussed.

The potential flow solution for non-breaking free surface waves is described by the velocity potential  $\phi$ , and surface elevation  $\eta$  [15]. The physical fluid velocities  $u_H$  are

defined by the gradient velocity potential:

$$(u_H, w) = (\nabla_H \phi, \partial_H \phi) \quad (2.41)$$

with  $\nabla_H = (\partial_x, \partial_y)$

The kinematics free surface condition can be expressed as follows:

$$\partial_t \eta = -\nabla_H \eta \cdot \nabla_H \tilde{\phi} + \tilde{w}(1 + \nabla \eta \cdot \nabla \eta) \quad (2.42)$$

where  $\tilde{\phi} = \phi(x, \eta)$  and  $\tilde{w} = (x, \eta)$

The Bernoulli equation for an unsteady fluid is found using the integrated momentum equation. Setting  $p = 0$  at  $z = \eta$ , the Bernoulli equation can be written as follows:

$$\partial_t \tilde{\phi} = -g\eta - \frac{1}{2}(\nabla_H \tilde{\phi} \cdot \nabla_H \tilde{\phi} - \tilde{w}^2(1 + \nabla \eta \cdot \nabla \eta)) \quad (2.43)$$

Equation 2.43 represents the dynamic free surface condition.

Since both equations 2.42 and 2.43 are nonlinear, a closed form solution does not exist. Therefore, the solution is approximated numerically in time using a Runge-Kutta method [16]. Here, the free surface vertical velocity,  $\tilde{w}$ , is found by deriving  $\phi$  from the Laplace equation:

$$\nabla_H^2 \phi + \partial_{zz} \phi = 0, \quad -h \leq z < \eta \quad (2.44)$$

The Laplace equation in equation 2.44 is solved:

$$\sigma = \frac{z + h(x)}{\eta(x, t) + h(x)} \quad (2.45)$$

The transformation of  $\sigma$  in equation 2.44, is used to transform a physical grid to computational grid in the sigma domain. Figure 2.11 illustrates that the computational grid is clustered around areas where largest gradients can be expected.

From equation 2.44 can be derived that the sigma transformation is only valid for a single valued  $\eta$  function. When wave breaking tends to occur the stability of the model is ensured by a filter which locally dissipates energy from the wave [16]. This breaking wave filter  $\gamma$  is based on the downward water particle acceleration and is activated for:

$$\frac{dw}{dt} \leq \gamma g, \quad \text{where } \gamma[0.3 - 1] \quad (2.46)$$

Finally, when  $\phi$  is known, the physical velocities can be obtained:



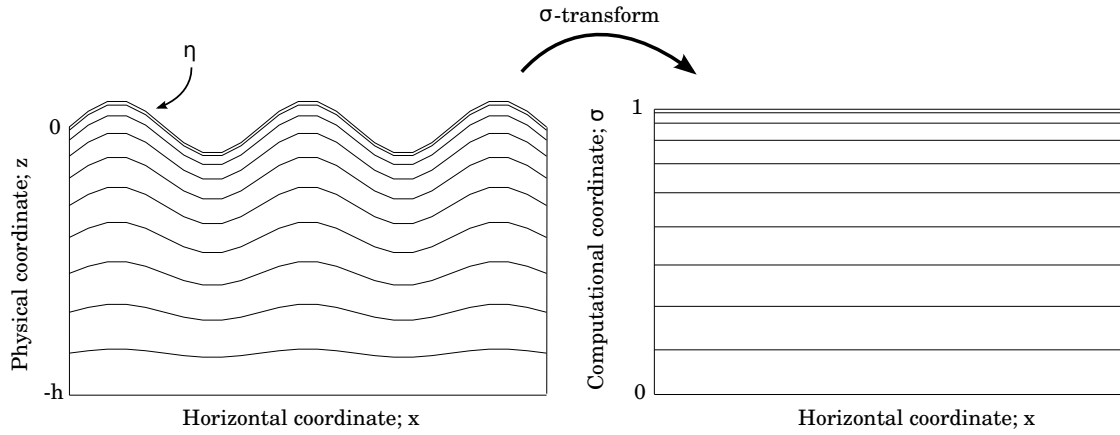


Figure 2.11: Sketch of the grid in physical coordinates and in the computational  $\sigma$ -domain [15].

$$u_H(x, z) = \nabla_H \phi(x, \sigma) + \nabla_H \sigma \partial_\sigma \phi(x, \sigma) \quad (2.47)$$

$$w(x, z) = \partial_\sigma \phi(x, \sigma) \partial_z \sigma \quad (2.48)$$

OceanWave3D is able to numerically reproduce sea states from measurements. To reproduce wave tank test in the potential flow solver, a time variable Neumann boundary condition is introduced [15]. This way, waves can be generated directly at the boundary. The boundary condition for the Laplace equation in 2.44, now becomes:

$$\frac{\partial \phi}{\partial x} = u \quad (2.49)$$

where  $u$  corresponds with the velocity of the wave paddle at the wave tank.

## 2.5. Wave analysis

An irregular sea state is composed of a superposition of multiple harmonic components. The crest heights and wave periods vary constantly over the time series. Figure 2.12 shows how the individual crest heights are identified in the time series.

It is common practice to use the downward zero crossing definition to characterise a single wave event. Herewith, the crest is preceded by a trough. This includes the steep front of the wave, which is especially relevant for breaking waves.

From the time series all the individual wave heights can be identified. A commonly used statistical indicator for a sea state is the significant wave height  $H_s$ , which is defined as the average of the highest one-third of the recorded waves.

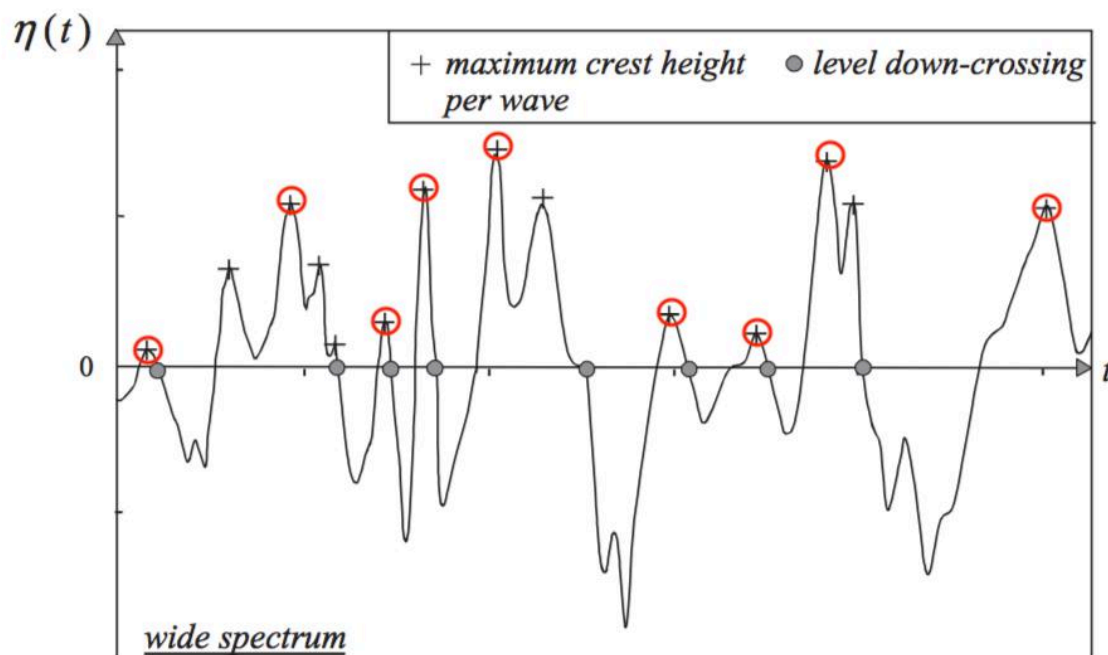


Figure 2.12: Maximum crest height and level down-crossing per wave, only one peak(encircled in red) per zero down crossing wave [10].

Besides of the evaluation of the wave recording in the time domain, the waves are further analysed in the frequency domain using the Fourier series analysis. Because in long term wave statistics the exact water level at a certain time is not really interesting, phases are discarded. The statistical properties of wave height and frequencies will suffice for analysis. Using the Fourier series analysis, one can obtain the energy density spectrum  $S(\omega)$ .

Deriving the moments of the area under the spectrum, results in the integral wave parameters  $m_n$ . The variance  $m_0$  of the sea surface elevation is given by  $0^{th}$  order moment.

Based on  $m_0$ , the significant wave height  $H_{m_0}$  can readily be derived:

$$H_{m_0} = 4\sqrt{m_0} \quad (2.50)$$

A commonly used wave spectrum is the JONSWAP wave spectrum [11]. It is based on measurement data collected in the North Sea and describes the spectral formulation for coastal wind generated waves.

For the numerical analysis of the time series in this thesis, WAFO is used. WAFO (Wave Analysis for Fatigue and Oceanography) is a Matlab toolbox for the statistical analysis of random waves and loads [2]. In WAFO one can identify and extract individual waves from a time series. These waves can be identified based on varies conditions, such as zero down crossing or up crossing. WAFO can make a statistical

analysis of the properties and analyse the individual wave heights and wave periods. Moreover, WAFO can be used to evaluate general properties of a sea state. In this thesis WAFO is used to identify the individual waves with corresponding wave height and wave period  $T$ . Additionally, using the spectral density spectrum,  $H_{m0}$  and wave peak period  $T_p$  are derived.



# 3

## Measurement data

Wave tank measurement used for this thesis were done within the Joint Industry Project WiFi (JIP-WiFi). The experiments were set up to improve the current design methods for offshore wind turbines loads, specifically relating to breaking waves. This section reviews the collected measurement data and methodology of the experiments. Additionally, different methods to identify breaking waves are introduced and discussed. This results in a comparison between the different methods.

### 3.1. Experimental set-up

The wave tank experiments were carried out at the Atlantic Basin at Deltares. For the experiments, two monopile scale models were placed in the wave tank, both equipped with multiple force and pressure sensors. During the tests the monopiles were exposed to series of wave trains. The irregular wave trains, with a total of approximately 5000 waves, created a large sample size needed for the experiment. To simplify the scale models, secondary steel was not included on the monopiles. The Atlantic Basin measures a length of 75m, a width of 8.7m and a water depth 1.2m. The two cylinders in the wave tank have diameters of 10cm (4.5m full scale) and 16cm (7.2m full scale). Figure 3.1 shows a general overview of the wave tank in action.

Since the experiments are done on a scaled model, all parameters have to be scaled. In the experiments a scale factor of 1:45 is used. Therefore, the wave height is scaled with a proportional scaling factor  $\alpha_L$  of 45. Similarly, wave period, pressures and forces can be scaled using Froude scaling. Scaling factors are shown in table 3.1. Within the experiments, the waves were modeled in fresh water instead of in salt water. The reduction in loading for salt water is scaled using  $\alpha_\rho$ . For comparison, all results shown in this thesis are unscaled.

Multiple wave gauges were placed throughout the wave tank to measure the surface elevation (see figure 3.2). Spreading the gauges around the basin, the wave elevation can be measured throughout the tank. This way, all the wave data can be collected

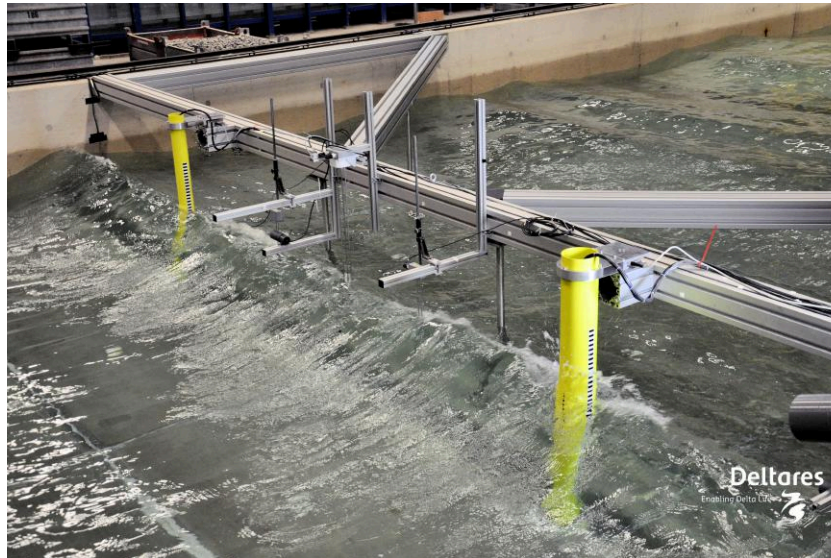


Figure 3.1: Monopile models situated in Atlantic Basin at Deltares with wave impacting the monopile.

Parameter	scaling factor
Wave height, $H$ [m]	$\alpha_L$
Wave period, $T$ [s]	$\sqrt{\alpha_L}$
Base shear, $F$ [N]	$\alpha_\rho \alpha_L^3$

Table 3.1: Froude scaling parameters

accurately. The wave gauge used as reference in this thesis is placed between the two monopiles. This ensures relatively undisturbed waves at the location of the monopile.

The monopile model structure is equipped with multiple pressure sensors. The sensors were placed on the impact area of the incoming wave. Due to the spreading of the sensors, impact pressures vary depending on the location of impact. Figure 3.3 shows the placement of the pressure sensors. The base shear is measured using force transducers at the bottom of the pile.

The waves in the basin are generated by the wave maker. This wave generator consists of a paddle going back and forth. Specifying the input of the wave paddle, one

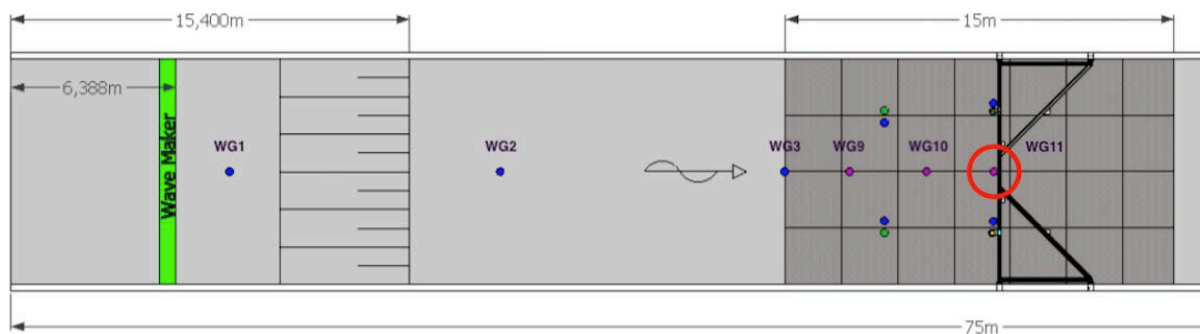


Figure 3.2: Locations of wave gauges placed in in the Atlantic basin. The location of WG 11 encircled in red.

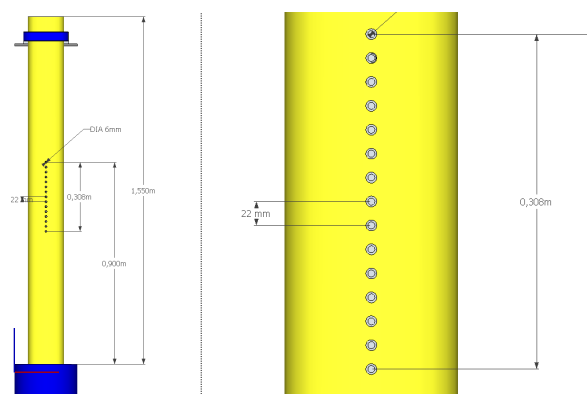


Figure 3.3: Locations of the pressure sensors on the monopile model placed in the Atlantic basin.

can generate the needed wave train. Furthermore, the water depth in the tank can be adjusted.

## 3.2. Data selection

For this thesis, since the main focus is on large diameter structures, only the measurements of the larger scale monopile are used. The wave tank tests are run on a flat seabed and without any current. Multiple runs were done to create a large sample size. All the runs shown in table 3.2 have approximately a 1000 wave events. The measured characteristics for the sea states are summarized in table 3.2.

Ref number	$H_{m0}$ [m]	$T_p$ [s]	$d$ [m]
A06a	0.2232	2.0184	0.6644
A06b	0.2185	2.0184	0.6644
A06c	0.2253	2.0588	0.6644
A06d	0.2212	1.9063	0.6644
A06e	0.2214	1.9423	0.6644

Table 3.2: Sea state parameters of wave tank tests. With significant wave height, peak period and water depth.

The main measurement results that are extracted for research in this thesis are as follows:

- Surface elevation
- Base shear

Surface elevation and base shear are further used in this research to extend the knowledge of breaking waves. In further sections of this thesis the measurements are evaluated and presented.

### 3.2.1. Identification of slamming waves

No visual inspection can be done on the wave data, hence the slamming waves have to be identified differently. Therefore, measurement data from the wave tank will be analysed numerically to identify a breaking wave. For the analysis of the wave trains the Matlab package WAFO is used. The Matlab package is further discussed in section 2.5. The numerical analysis of the waves calls for a breaking wave definition. A slamming wave event is defined [13] as follows:

- Front crest steepness  $S$  should reach breaking limit
- The slamming impact of the wave should be more than 4 times standard deviation of the force series

To have a numerical identification method of breaking waves, a new method is introduced. Here both the load of the breaking wave and the shape of the breaking wave are combined to analyse the sea state. A method to describe the wave shape is the crest front steepness. Crest front steepness  $S$  is given by  $S = \frac{\eta}{\lambda'}$ . Where  $\eta$  is the crest height and  $\lambda'$  the crest front wavelength. A breaking limit is found at crest front steepness  $S > 0.2$  [13]. This criterion combined with a significant load increase in the time series results in the following breaking wave identification method: The statements above can be summarised in equations 3.5 and 3.6.

$$S_b > 0.2 \quad (3.1)$$

$$F_b \geq 4\sigma_F \quad (3.2)$$

where  $S_b$  is front crest steepness for breaking wave and  $F_b$  is impact loading of breaking wave.



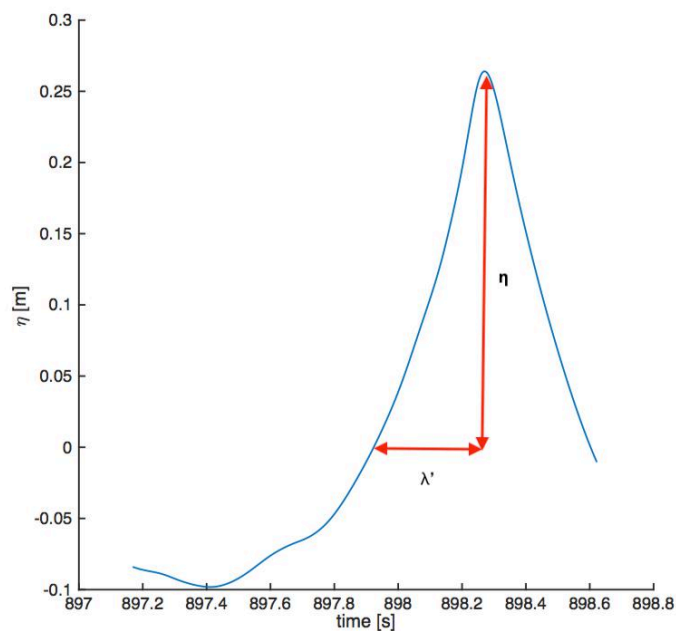


Figure 3.4: Front crest steepness  $S = \frac{\eta}{\lambda'}$  definition. With  $\eta$  is the crest height and  $\lambda'$  the crest front wavelength.

This means that a slamming impact on the monopile is not only identified as an impact from a breaking wave, but additionally, the forces have to be significantly larger. Figure 3.5 shows a plotted time series for wave elevation and base shear in which the breaking waves are indicated with triangles. For the identification of the slamming wave event, the afore mentioned criteria were used. In appendix A one can find all the measurement data plots with indicated slam events.

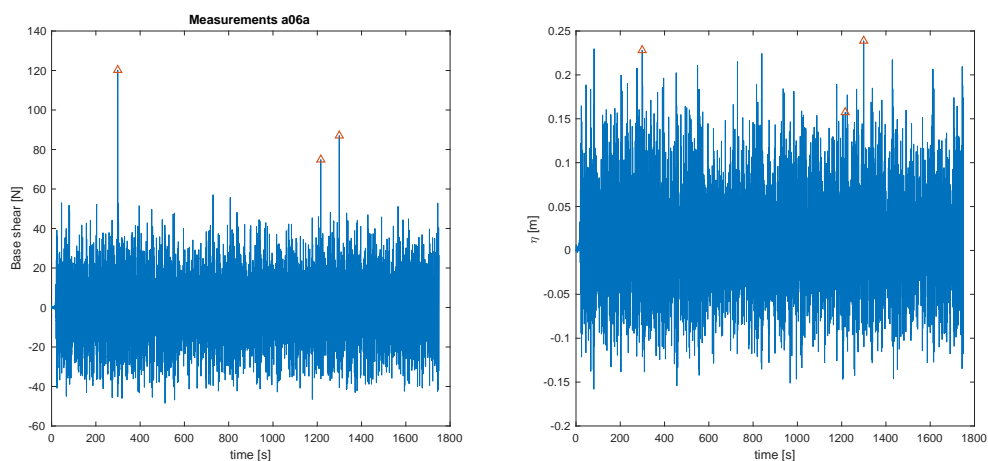


Figure 3.5: Measurement time series for case A06a. Left graph shows base shear and right graph shows wave elevation. Slamming wave events are indicated with red triangle.

### 3.2.2. Identification of slamming waves ECN

ECN introduced a different method to identify breaking waves. Instead of looking at the slam load caused by the breaking wave, ECN determines a breaking wave based on both wave height and wave period:

$$H_b > 1.4H_{m0} \quad (3.3)$$

$$0.9T_p \leq T_b \leq 1.1T_p \quad (3.4)$$

where  $H_b$  is breaking wave height,  $H_{m0}$  significant wave height,  $T_p$  peak period and  $T_b$  wave period of breaking wave.

Using the above mentioned criteria for breaking waves and the same time series as in section 3.2.1, figure 3.6 was plotted. From this plot it can be noted that the ECN identification method identifies different waves as breaking and potentially miss high slam loads caused by breaking waves. This is due to the fact that ECN solely focuses on wave height and a significant load increase of a slamming wave impact is not considered.

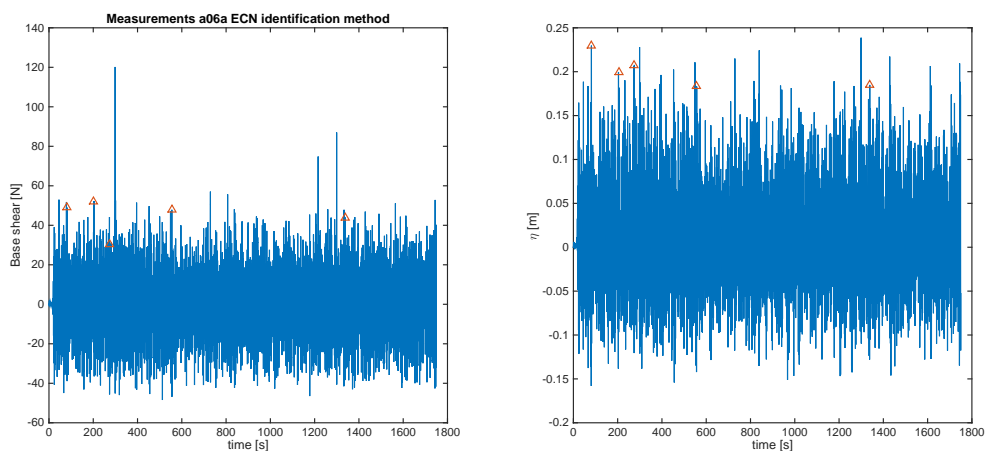


Figure 3.6: Measurement time series for case A06a. Left graph shows base shear and right graph shows wave elevation. Slamming wave events are indicated with red triangle. ECN-ID method.

## 3.3. Processing

All measurement wave events from test A06 summarised in figure 3.7, where the slamming waves are indicated in red. Looking at both graphs, it can be seen that not all high waves will necessarily break. Furthermore it can be noted, when focussing on 3.7b, that the high peak forces on the monopile are identified as breaking waves.

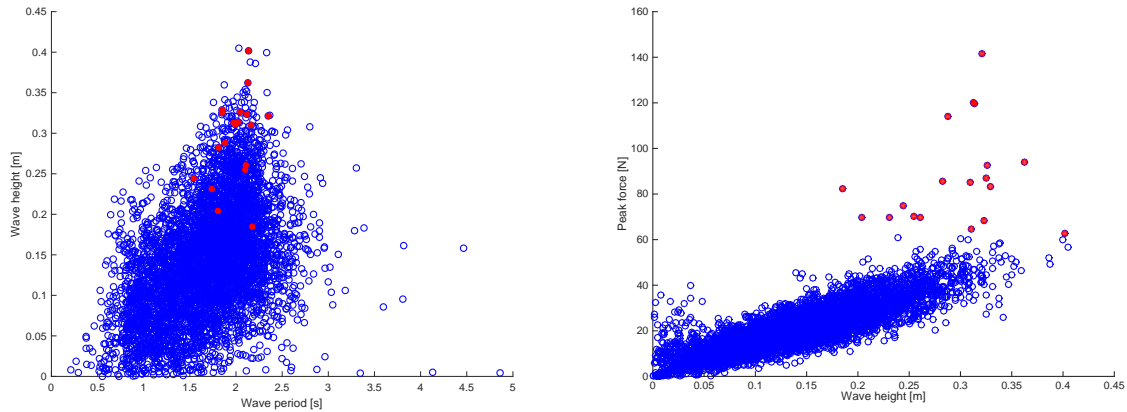
(a)  $H$  and  $T$ (b)  $H$  and  $F_p$ 

Figure 3.7: Scatter plot for all A06 measurements series. Slamming waves are indicated in red.

What was already noted in section 3.2.2, is that the ECN-ID method misses high slam loads on the monopile. In figure 3.8b, it can be seen that indeed the identified breaking waves are high, but do not necessarily have high slamming impact. Therefore it can be concluded that this method falls short in filtering the high slamming waves. The method as described in 3.2.1 does identify the high slam loads as breaking waves because it considers impact forces. Thus, resulting in a better suited identification method.

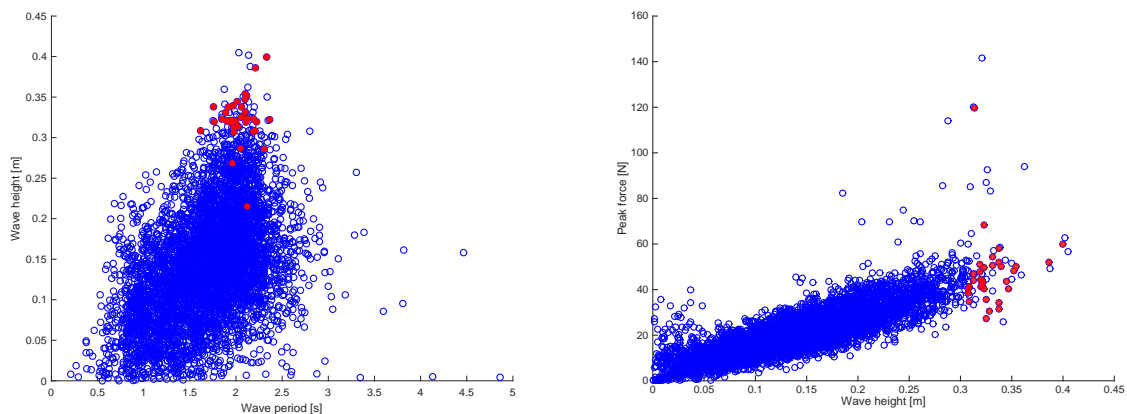
(a)  $H$  and  $T$ (b)  $H$  and  $F_p$ 

Figure 3.8: Scatter plot for all A06 measurement series. ECN-ID slamming waves are indicated in red.

### 3.4. Summary

This chapter reviews the measurement campaign for the WiFi JIP. The focus for the measurements was breaking waves on monopiles. Using scripts, the wave data was analysed and breaking waves identified numerically. Different ID methods are described and compared throughout this chapter. It is shown that the ECN-ID method

misses high peak loads and is therefore unusable for further analysis. Hence it was chosen to continue with the alternate ID method. Below, the slam identification criteria are outlined once more:

$$S_b > 0.2 \quad (3.5)$$

$$F_b \geq 4\sigma_F \quad (3.6)$$

The above statements are used to identify potential slamming waves further in this thesis.

# 4

## Numerical wave modelling

The following chapter focusses on the numerical propagation of waves. This is done using the aforementioned non-linear potential flow solver OceanWave3D. Based on the measurement data described in chapter 3, the wave characteristics from test A06 were tried to reproduce. The newly generated sea state is then compared to the measurement data.

### 4.1. Set-up numerical wave tank

The wave tank where the measurements took place, the Atlantic basin at Deltares, was recreated in numerical model of OceanWave3D. The Atlantic basin is relatively wide, hence interactions with the sides can be neglected and a 2 dimensional model can therefore be used. The numerical model uses a wave generation zone and a zone where wave are absorbed. Figure 4.1 shows the general lay-out of the numerical wave tank in OceanWave3D. The wave tank built in OceanWave3D uses the dimensions of the Atlantic basin at Deltares. Appendix C shows an example of an input file used to operate OceanWave3D. The modelled wave input is based on the unscaled measurement data from the experiments within the WiFi project. In table 4.1 the dimensions and general input for the numerical model are given.

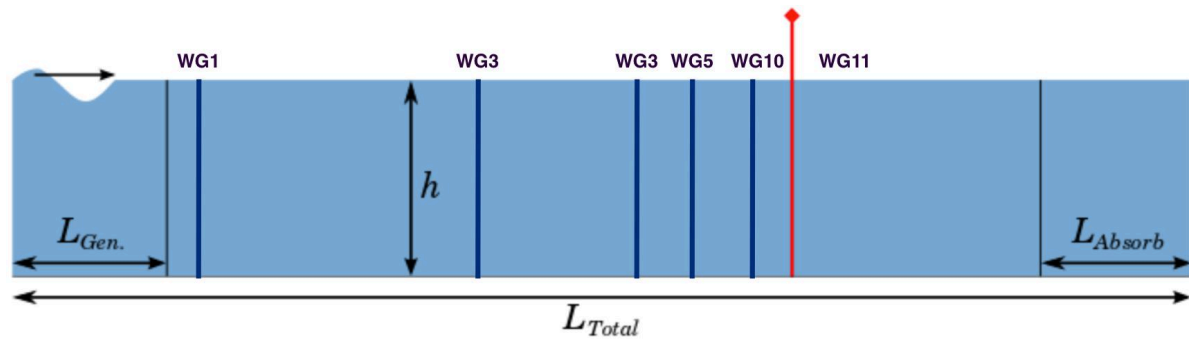


Figure 4.1: Numerical representation of Atlantic basin in potential flow solver OceanWave3D, with placement of wave gauges throughout the wave tank and red bar indicating location of fictive monopile.

The wave data gathering points in the numerical model are put exactly in the same place as the wave gauges in the Atlantic basin, see figure 4.1. Wave gauge 11, which was used for reference in the measurement results, is also the main measurement point in the OceanWave3D model. Wave gauge 11 is placed between the two monopiles in the wave tank and represents the location of the monopile in the numerical model. The potential flow solver itself does not contain a monopile model, so no structure interaction is present in the solver. However, within the Morison equation the structure interaction is included in the calculation. At the reference points in the numerical model the wave kinematics are gathered and will be shown for several cases later in this chapter.

Input parameter	Value
$L_{total}$ [m]	75
$L_{gen}$ [m]	15
$L_{absorb}$ [m]	15
$h$ [m]	0.664
$n_x$	1001
$n_y$	1
$n_z$	11
$dx$	0.75
$dt$	0.04

Table 4.1: Input parameters describing the Atlantic basin wave tank in OceanWave3D.

## 4.2. Validate numerical wave tank

To test the validity of the wave tank numerical cell density, a grid study was performed. Using the input parameters from table 4.1, different cell sizes were tried in the numerical modelling. Table 4.2 gives the points per wavelength(ppwl) and corresponding total number of cells in the numerical model.

Ref number	Cell size $dx$ [m]	ppwl $n_L$	Number of cells $n_x$
res05	0.75	5	101
res10	0.4	10	191
res20	0.2	20	376
res60	0.075	60	1001

Table 4.2: Different grid resolutions with corresponding reference number used as input for grid test.

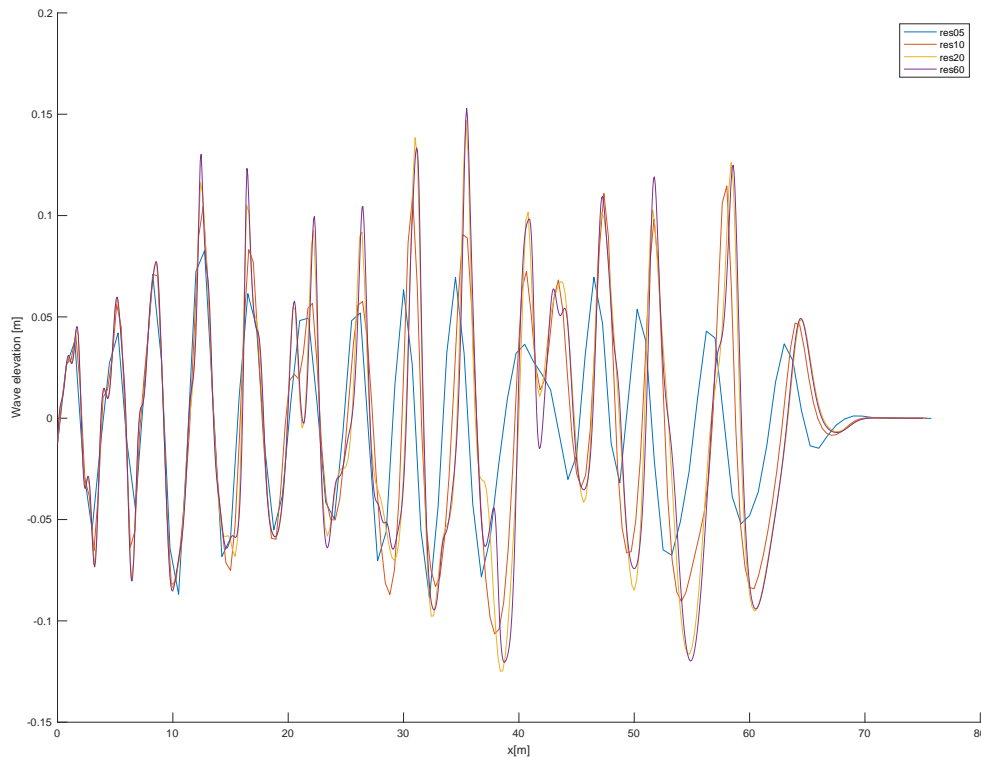


Figure 4.2: OceanWave3D test run with varying grid resolutions. Plotted are res05, res10, res20 and res60.

Comparing free surface elevation of the different cell densities plotted in figure 4.2, it can be noted that with increasing density, the wave is represented in more detail. Relatively large differences in accuracy between low and high resolution can be seen in the higher and steeper waves. Since the focus of this thesis is mainly on those high and steep waves it is needed to do the computations with a high density grid of 60 points per wave length.

To ensure numerical stability and accuracy of the model, the Courant–Friedrichs–Lewy (CFL) condition has to be met. Shown in 4.1, is the CFL condition for the potential flow solver OceanWave3D. The CFL condition is needed for convergence of partial differential equations in the numerical solver. For stable and accurate results the CFL number needs to be less than or equal to 1.

$$CFL = \frac{u_{max} \cdot dt}{dx} = \frac{\sqrt{\frac{g}{h}} H_{max} \cdot dt}{dx} = \frac{\sqrt{\frac{g}{h}} 1.86 H_s \cdot dt}{dx} \leq 1 \quad (4.1)$$

where  $u_{max}$  is the maximum horizontal velocity,  $dt$  is the time step size and  $dx$  the spatial resolution. The input of res60 in table 4.2, meets the criterion of  $CFL \leq 1$ .

### 4.3. Select input sea state

As explained in section 2.4, the potential flow solver OceanWave3D is capable of regenerating wave elevation from measurements tests. However, unfortunately no wave paddle input signals were available for the measurements performed for the WiFi project. Therefore, a direct copy of the results was not feasible using OceanWave3D. Instead the the build-in option in the OceanWave3D software of generating a new state was used. In the upcoming sections a sea state which is similar to the measurements is generated by the potential flow solver. Based on a JONSWAP spectrum and using the sea state parameters of the measurements as input the waves are generated.

The initial input for the numerical wave tank is taken from the measurements results as presented in chapter 3. The significant wave height and the peak period are extracted from the measurement time series. For the first model, the significant wave height and peak period are governing. Input parameters for the numerical model are given in table 4.3.

Ref number	$H_{m0}$ [m]	$T_p$ [s]
A06a-Measurements	0.2232	2.0184
A06b-Measurements	0.2185	2.0184
A06c-Measurements	0.2253	2.0588
A06d-Measurements	0.2212	1.9063
A06e-Measurements	0.2214	1.9423

Table 4.3: Sea state parameters from wave tank tests A06-Measurements in Atlantic basin.

Using the OceanWave3D and input parameters for the wave tank from table 4.1 and the sea state parameters for the JONSWAP spectrum from table 4.3, 5 different sea states with approximately 1000 waves are generated. To make a proper comparison between A06-Measurements and A06-OCW3D, all wave events are plotted in a Rayleigh distribution. This allows for comparison between the different sea states. This results in the following Rayleigh distribution plot in figure 4.3.

From figure 4.3 can be seen that generally waves from the measurements are higher than from the numerical model. This shows that wave energy in the numerical wave tank is dissipated. Dissipation of wave energy results in lower waves further down in the tank. Due to the losses, the input significant wave height should be raised to be able to match the desired values as compared to the measurement results.

First, it is checked how much wave energy is dissipated in the potential flow solver.



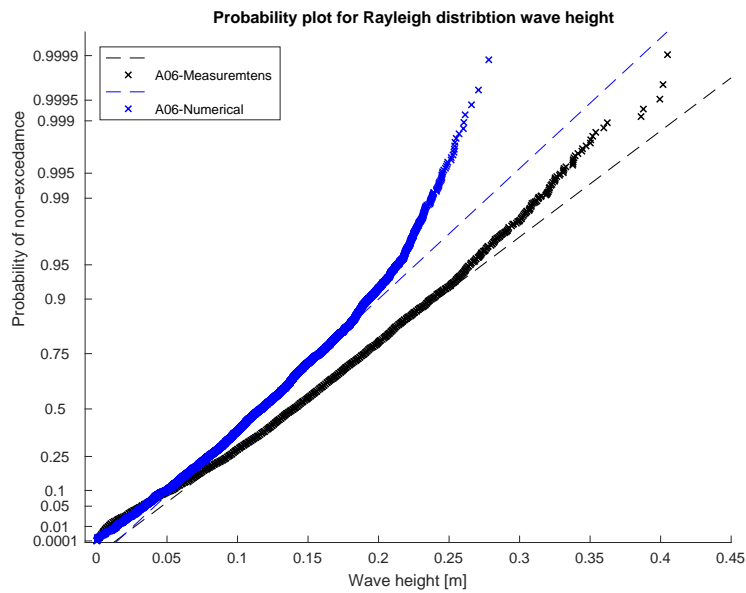


Figure 4.3: Accumulated OceanWave3D wave events for all A06 cases compared with wave events from measurement-a06.

The input and recorded significant wave heights from case A06-OCW3D which are presented in table 4.4, show that indeed energy is dissipated in the model and therefore a reduced significant wave height is recorded at reference point wave gauge 11.

Ref number	$H_{m0}$ input [m]	$H_{m0}$ at wg11 [s]	Breaking filter $\gamma$
A06a-OCW3D	0.2232	0.1826	0.3
A06b-OCW3D	0.2185	0.1806	0.3
A06c-OCW3D	0.2253	0.1849	0.3
A06d-OCW3D	0.2212	0.1782	0.3
A06e-OCW3D	0.2214	0.1789	0.3

Table 4.4: Wave energy dissipation check for 06a-OCW3D in the numerical wave tank. Comparing  $H_{m0}$  at the input and at the location of the monopile.

Dissipation of energy in the numerical model is done by the breaking wave filter  $\gamma$  as introduced in section 2.4. Through an iterative process the fitting input parameters are obtained. Shown in table 4.5 is the iterative process to identify the needed significant wave height input in the JONSWAP model to obtain a matching  $H_s$  at wave gauge 11.

Ref number	$H_{m0}$ input [m]	$H_{m0}$ at wg11 [s]	Breaking filter $\gamma$
S01	0.2230	0.1959	0.7
S02	0.2480	0.2138	0.7
S03	0.2520	0.2163	0.7
S04	0.2600	0.2260	1.0
S05	0.2600	0.2280	0.7

Table 4.5: Wave energy dissipation check for S01 in the numerical wave tank. Comparing  $H_{m0}$  at the input and at the location of the monopile.

As can be seen in figure 4.4, case S05 shows good correspondence with the measurement results. S05 and A06-Measurements are well aligned. Only for some extreme waves the the wave height is not matched. This is due to the built-in dissipation of energy in OceanWave3D when wave particle accelerations are to high. Nonetheless, S05 shows much comparability. Thus the sea state input parameters of S05 are taken as input for further numerical models.

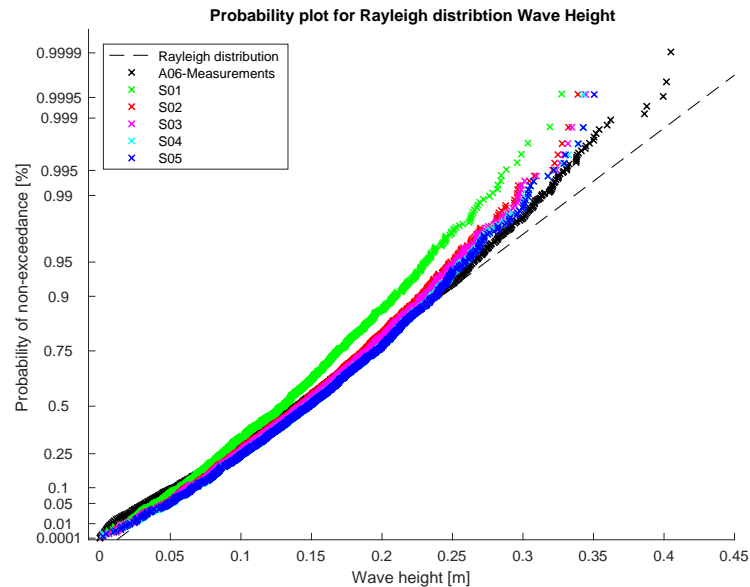


Figure 4.4: Accumulated OceanWave3D wave events for all A06 cases compared with wave events from A06-Measurements.

Since in table 4.5 only the significant wave height at the monopile was compared, an additional check is to be done. To be sure that the numerical wave tank is comparable to the actual one, the dissipation is checked throughout the tank. By comparing the significant wave heights collected from the wave gauges in the wave tank to the significant wave heights recorded in the numerical model of S05, the dissipation is checked. Table 4.6 shows the significant wave height for the A06a-measurements and and S05. As can be noted from table 4.6, both sea states show comparable dissipation in the tank. Additionally, the peak period lies within the range of the different measurement tests as shown in table 4.3. Moreover, both in the numerical model as in the measurements, the peak period tends to increase further in the wave tank.

Wave gauge #	1	2	3	9	10	11
<b>A06-Measurements</b>						
$H_{m0}$ [m]	0.251	0.235	0.219	0.225	0.218	0.224
$T_p$ [s]	1.932	1.932	1.932	1.969	1.969	1.969
<b>S05</b>						
$H_{m0}$ [m]	0.249	0.240	0.229	0.228	0.228	0.228
$T_p$ [s]	2.074	2.101	2.128	2.128	2.156	2.156

Table 4.6: Wave energy dissipation check for S05 in the numerical wave tank. Comparing  $H_{m0}$  on multiple locations throughout the wave tank.

## 4.4. Long numerical model

To create a large sample size of potential slamming waves, a sea state was generated with approximately 10.000 waves. This way, more potential slamming waves are generated and allow for good comparison.

Based on the developed and verified model S05, a larger sample size sea state was generated. It uses the same sea state input characteristics, but with more generated waves. Displayed in figure 4.5 is the generated sea state L03 plotted in a Rayleigh distribution along with the measured wave heights from the wave tank tests. As can be noted, the generated sea state suits the measurements well, only extreme high waves are less well interpreted and slightly underestimated.

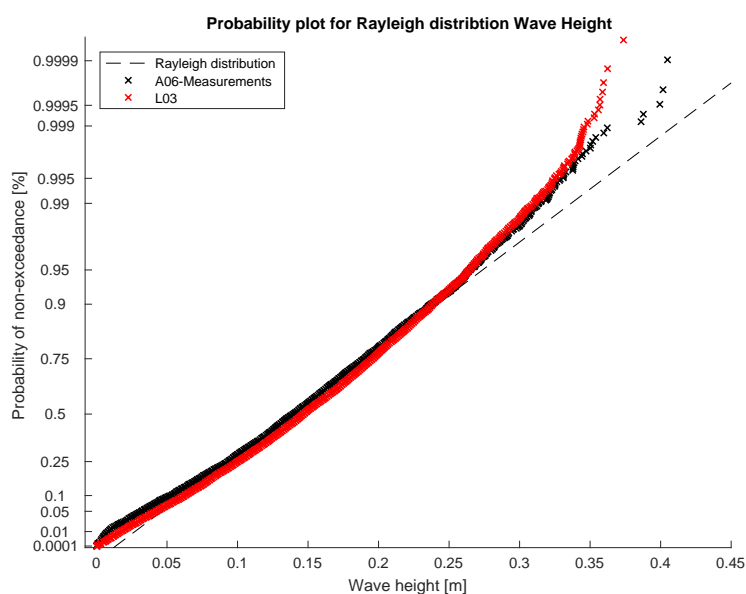


Figure 4.5: Probability plot with Rayleigh distribution for wave heights from A06-measurements and L03 sea states.

## 4.5. Summary

In this chapter a numerical model was introduced to describe the sea state from the measurements campaign in OceanWave3D. At first, the generated sea state appeared to lack the necessary wave height. By adjusting the input for the JONSWAP model, a sea state was found that matches the measurements. Wave energy dissipation is checked throughout the measurements wave tank and compared to dissipation in the numerical model. It was shown that both the wave tank and numerical model show resembling dissipation. The findings are summarised in table 4.7. Sea state L03 will be used for further analysis in this thesis.

Ref number	$H_{m0}$ [m]	$T_p$ [s]	$d$ [m]	$\gamma$ [-]	duration [s]	no. of waves
L03	0.260	2.0184	0.6644	0.7	20.000	10.000

Table 4.7: Summary of sea state input parameters for numerical simulation L03.

# 5

## Impact loading in numerical model

In the upcoming sections, the numerically generated sea states from chapter 4 are used to calculate wave and slam loading on the monopile. This is compared to measurements from the wave tank tests. The chapter has the following objectives:

- Compute wave force on monopile
- Identify potential slamming waves
- Define numerical slam load representation to fit measurements

### 5.1. Wave loading on monopile

For estimation of the wave induced forces acting on the monopile, the Morison equation is used. As referred to in section 2.2, the Morison equation gives a good approximation of the wave loads on slender cylindrical structures. The loads are calculated based on the wave kinematics found in the numerical OceanWave3D model L03 developed in chapter 4. The Morison equations is as follows:

$$F_m(t) = C_m \rho \frac{\pi}{4} D^2 \dot{u}(t) + C_d \frac{1}{2} \rho D u(t) |u(t)| \quad (5.1)$$

Wave kinematics in the OceanWave3D model are collected in 11 locations on the z-axis. Computation of the wave load is done by interpolating between 2 collection points. Hence the wave load will be calculated in 10 different parts along the monopile. To enhance accuracy of the potential flow solver, the grid points are more clustered at the free surface as can be seen in figure 2.11.

### 5.1.1. Force coefficients

Since particle velocities and accelerations at the monopile can be derived from the numerical model, only the inertia and drag coefficients  $C_m$  and  $C_d$  are to be determined separately. The force coefficients are dependent on the non-dimensional parameters Keulegan-Carpenter and Reynolds number.

$$KC = \frac{u_{max}T}{D} \quad (5.2)$$

$$Re = \frac{u_{max}D}{\nu} \quad (5.3)$$

with  $u_{max}$  the maximum horizontal velocity at still water level,  $T$  the wave period,  $D$  monopile diameter and  $\nu$  the kinematic viscosity for water.

With a recorded  $u_{max}$  of 1.2 m/s for the generated sea state L03,  $D = 0.16$  m,  $T = 2.1$  s and  $\nu = 1.0 \cdot 10^{-6}$  m<sup>2</sup>/s it is calculated that  $KC \approx 16$  and  $Re = 2.0 \cdot 10^5$ . This can be used to calculate the drag and inertia coefficients. The determination of  $C_m$  and  $C_d$  is done following the DNV guidelines for offshore wind turbines.

$$C_m = \text{Max} \begin{cases} 2.0 - 0.044(KC - 3) \\ 1.6 - (C_{DS} - 0.65) \end{cases} \quad (5.4)$$

where  $C_{DS}$  is 0.65 for a smooth cylinder.

$$C_d = C_{DS}\psi(C_{DS}, KC) \quad (5.5)$$

with wake amplification factor  $\psi$  to be extracted from figure 5.1.

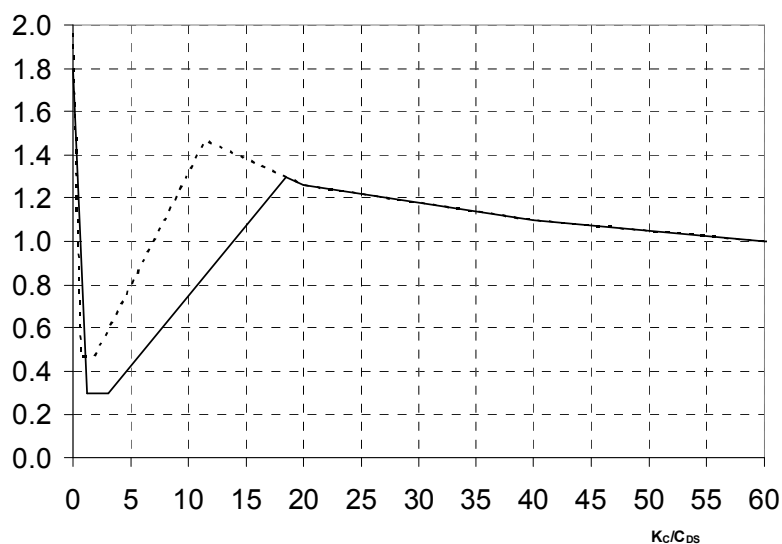


Figure 5.1: Wake amplification factor as function of KC number for smooth (solid line) and rough (dotted line) [5].

By means of using the definitions as stated in DNV RP-C205 [5],  $C_m$  and  $C_d$  are estimated at 1.6 and 0.78 respectively. The results are summarised in table 5.1. The force coefficients are kept constant over the entire water depth.

$Re$	$KC$	$C_d$	$C_m$
$2.0 \cdot 10^5$	16	0.78	1.6

Table 5.1: Reynolds number and Keulegan-Carpenter number with corresponding force coefficient for L03.

### 5.1.2. Wave loading

Based on the Morison equation as in equation 5.1 and with force coefficient as defined in table 5.1, the following Rayleigh distribution can be plotted:

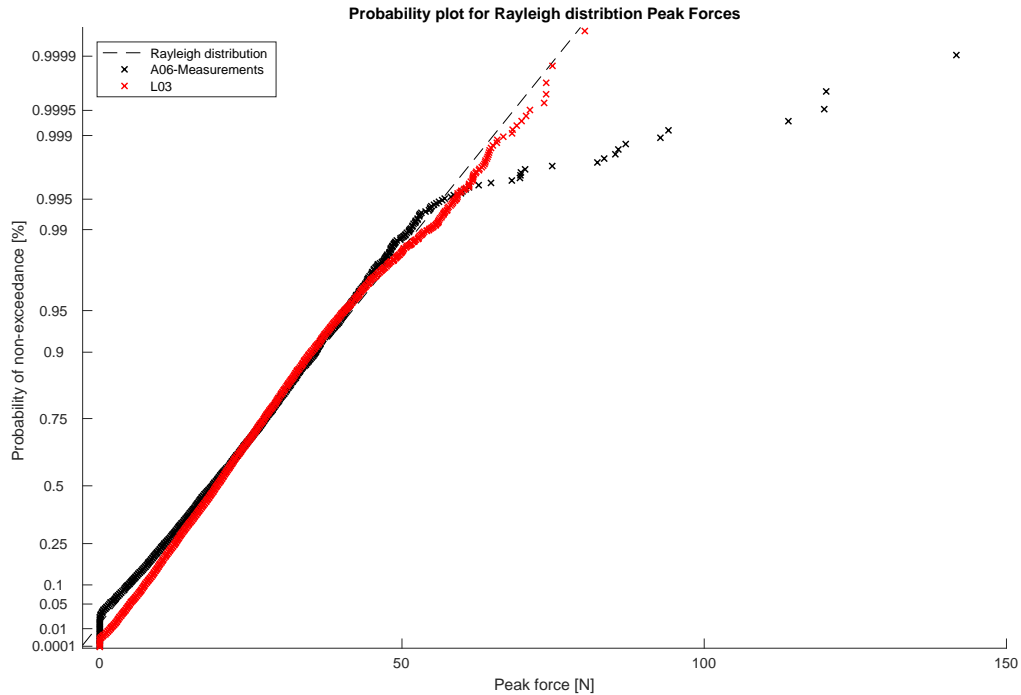


Figure 5.2: Probability plot with Rayleigh distribution for wave loading on the monopile from A06-measurements and L03 sea states.

When looking at the graph, it can be seen that the loads on the monopile, which are based on the numerically generated sea state L03, follow the measurements of A06 accurately. Only for waves with higher peak forces, the loads are under estimated. This difference in loading is explainable since the OceanWave3D model and the used Morison equation do not account for breaking waves. Whereas the measurements from the experiment clearly show a significant load increase due to slamming. Hence extreme loads for L03 will be lower than the measurements.

## 5.2. Identify potential slam waves

In the previous section it is shown that the load estimations are accurate for non-slamming waves, the next step is to identify the potential slamming waves. The identification of potential slamming waves is based on the criteria introduced in section 3.2.1:

$$S_b > 0.2 \quad (5.6)$$

$$F_b \geq 4\sigma_F \quad (5.7)$$



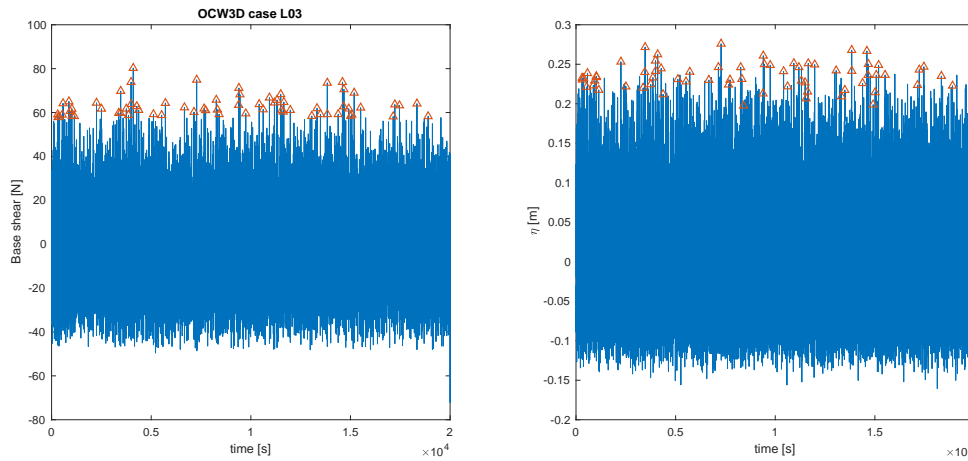
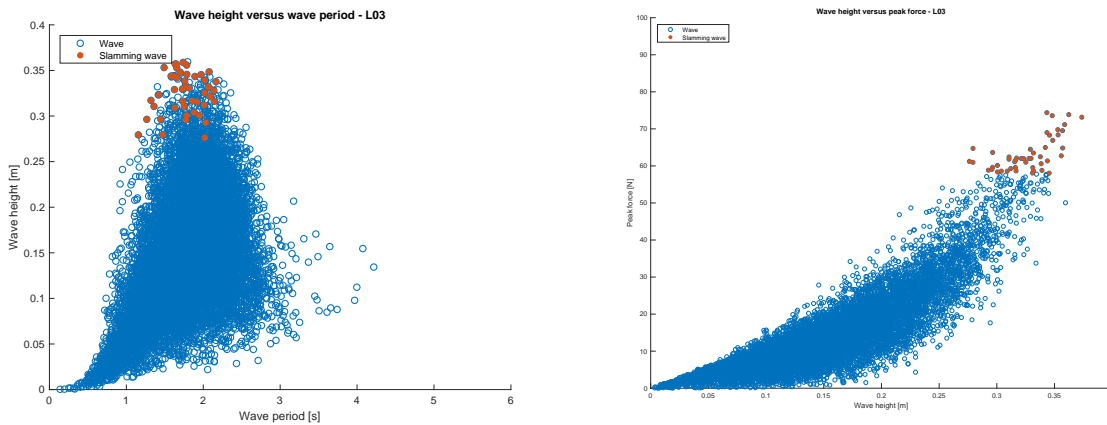


Figure 5.3: OceanWave3D time series for case L03. Left graph shows base shear and right graph shows wave elevation. Slamming wave events are indicated with red triangle.



(a)  $H$  and  $T$

(b)  $H$  and  $F_p$

Figure 5.4: Scatter plot for L03 OceanWave3D series. Slamming waves are indicated in red.

From the approximately 10.000 wave events in case L03, a total of 48 are identified as potential breaking waves were identified in time series L03.

### 5.3. Slamming wave load

As stated in section 5.2, the underestimating of the loads on breaking waves is due to the absence of a slamming part in the calculations the Morison equation. To adjust for this error, a slamming impact load is to be added. As introduced in section 2.3, the slam load can be added to the total force estimated by the Morison equation.

$$F = F_{inertia} + F_{drag} + F_{slam} \tag{5.8}$$

Since  $F_{inertia}$  and  $F_{drag}$  are calculated in the previous section,  $F_{slam}$  will be derived based on equations developed in section 2.3. The slamming force component will only be added to the waves which are identified as potentially slamming.

$$F_{slam} = \frac{1}{2}\rho C_s A u^2 \quad (5.9)$$

Where  $\rho$  is the water density, slamming impact area  $A$  is taken to be as presented by Paulsen et al. [17],  $A = \lambda H_b D \frac{2}{\pi^2}$ , with curling factor  $\lambda = 0.29 \frac{H_b}{H_s}$ . Slam coefficient  $A$  and impact velocity  $u$  are addressed in next sections.

### 5.3.1. Slam coefficient

In section 2.3 a general slamming coefficient was introduced. Here, the general slamming coefficient of  $C_s = 2\pi$  is verified against the measurements.  $C_s$  is to be derived from the experimental data as follows:

$$C_s = \frac{F_{slam}}{\frac{1}{2}\rho A u^2} \quad (5.10)$$

Since no water particle velocity is recorded in the experiments, the horizontal velocity is approximated by  $u = \sqrt{gh}$ . Based on the slam loads retrieved from the measurement campaign, the slam coefficients are calculated. Shown in figure 5.5 are the slam coefficients for all A06-measurements cases.

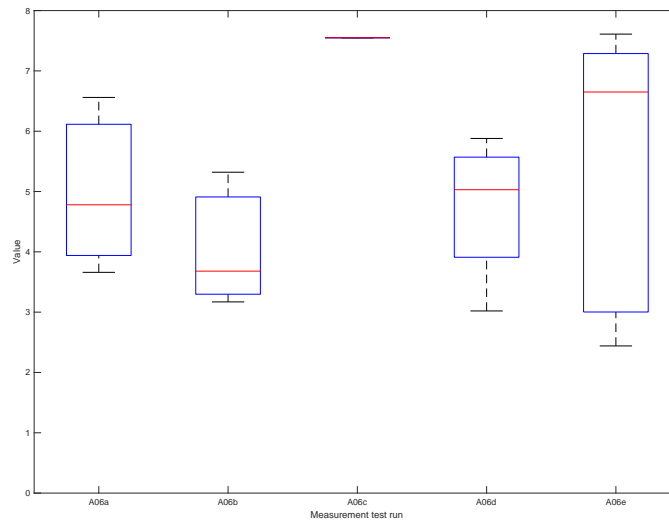


Figure 5.5: Boxplot indicating the range of slam coefficients for A06-Measurement.

The mean  $C_s$  values range around 5 - 7, for further calculations the value of  $2\pi$  is used in this thesis. A slamming coefficient of  $2\pi$  was already introduced in section 2.3

by both DNV and Paulsen et al.

### 5.3.2. Impact velocity

The horizontal velocity impacting the monopile structure is of great importance to the slam load formulation. As stated in section 2.3.2, different impact velocities are considered. Where DNV uses  $u = 1.1 \frac{\lambda}{T_b}$ , Paulsen et al. use  $u = \sqrt{gh}$ . This means that for a generated sea state, only one slamming wave impact velocity is used.

Since the potential flow solver OceanWave3D gives kinematics at the reference points and monopile, horizontal velocities can be extracted from the numerical model. This thesis uses the horizontal particle velocity at free surface for an individual slamming wave as calculated by the numerical model. This ensures an accurate estimation of slamming impact loading.

For DNV, the calculated impact velocity is 2.43 m/s, whereas the impact velocity for Paulsen et al. is 2.55 m/s. The impact velocity for the individual slamming wave range from 1.22 to 1.65 m/s.

### 5.3.3. Numerical slam load results

Now the slam load parameters are established and can be calculated according to equation 5.9, the slam forces for case L03 are added to the Morison forces. This slam load is only added to the waves which are identified as potential slamming waves. The results of the slam load calculation are graphically presented in figure 5.6. Here it is shown how the slamming wave impact is added to the Morison hydrodynamic forces.

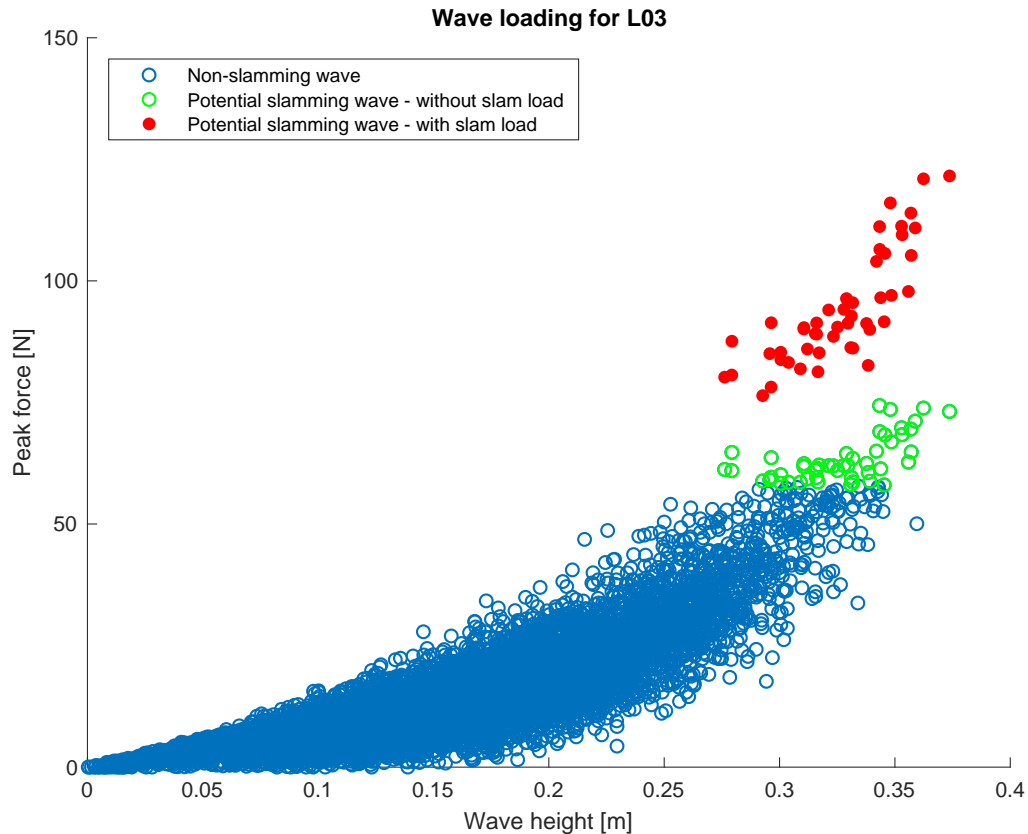


Figure 5.6: Scatter plot for all wave events of case L03. Green dots are wave identified as potential slamming waves and red dots represent the wave with added slam load.

To compare the calculated impact loading from the numerical model to the loads as measured in the wave tank, the forces are plotted in a probability plot. Figure 5.7 shows the calculated slam load along with the measurement impact loads. Here it can be observed how L03-without slam load- does not include the high peak loads and misses the high slam loads. Whereas L03-with slam load- follows the measurements from the wave tank closely. An other comparison is made in figure 5.8, where the different slam load representations of the numerical model are plotted. As described in section 5.3.2, methods differ in their impact velocity computation. From this figure it can be noted that methods from DNV and Paulsen et al. are more conservative in their load estimation. This difference is caused by the alternate impact velocities which are lower.

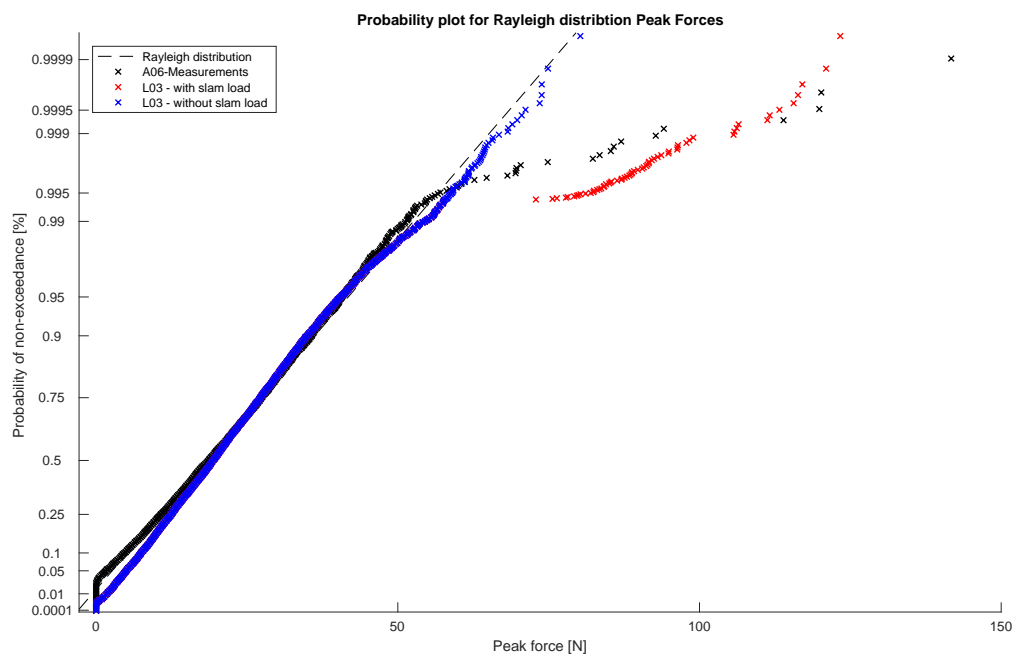


Figure 5.7: Probability plot for wave impact comparing A06-measurements to L03, with and without slam load.

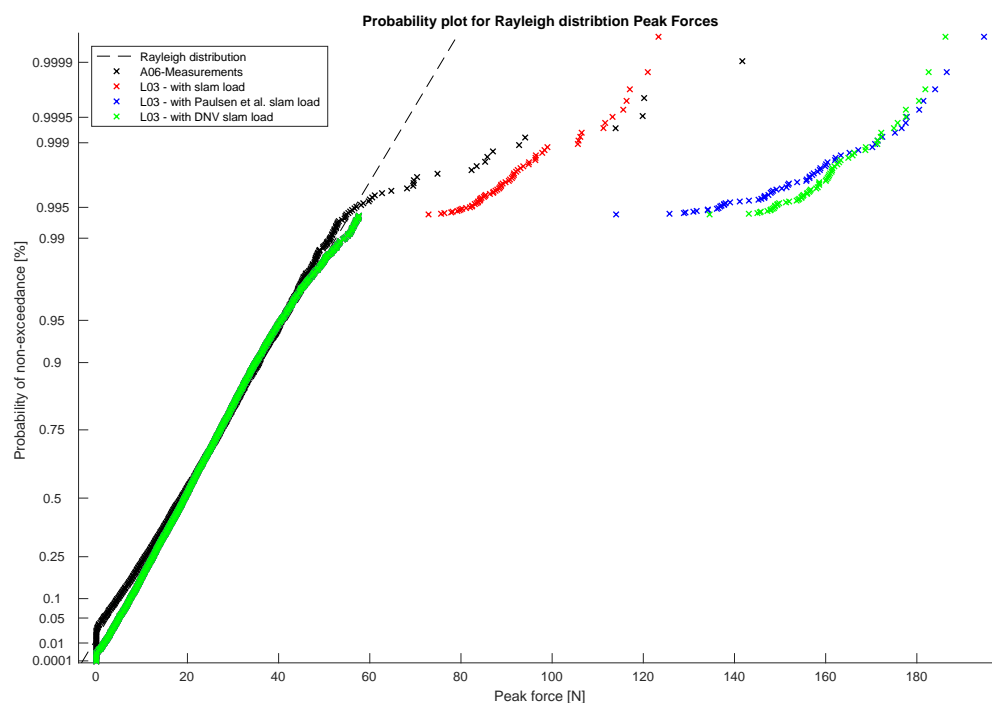


Figure 5.8: Probability plot for wave impact comparing A06-measurements to L03 with different slam load representations.

## 5.4. Summary

This chapter has addressed the computational steps required to estimate slam forces from a numerically generated sea state.

First the Morison loading on the monopile is assessed using the kinematics obtained from the OceanWave3D model. Based on the kinematics, the force coefficients are calculated applying DNV guidelines. Comparing the calculated wave impacts to the measurements, for non-slamming waves large similarity in wave loads was shown. Using the identification method for slamming waves based on steepness and impact force, waves are classified as potential slamming. Then, an additional slam load is added to the Morison force, which only applicable for the identified waves. The added slam load is calculated using the wave kinematics from OceanWave3D and uses momentum theory to establish the impact on the structure. The impact velocities of the incoming slamming waves are extracted for each slamming wave individually. Finally, the identification method results in a less conservative calculation method for impact slam loading.

# Conclusions and recommendations

## 6.1. Conclusions

The goal for this thesis was to establish an enhanced breaking wave model to identify the effects of breaking waves on monopile structures. Using wave measurement data from wave tank tests performed for the joint industry research project WiFi at the Atlantic basin with Deltares, different slam load representations are compared.

Based on measurement data an identification method was introduced to identify potential slamming waves from the time series. The numerical identification of potential slamming waves can later be used to mark waves in the potential flow solver. Based on impact force and wave shape, all waves in the time series are evaluated and following the criteria, some are identified as potential slamming.

Using the potential flow solver OceanWave3D, a numerical model to represent measurement data was developed and validated against measurement data. Dissipation in the numerical wave tank is compared to measurement results. It was shown that the developed sea states have comparable characteristics to the measurements. Using this, a proper comparison could be made between impact loads from both measurements and the numerical model. It was shown that for non-slamming waves, loads calculated using the numerical model are of comparable magnitude to the measurement results. Since the numerical model did not account for slamming wave impacts initially, an extra slam load is added later.

Based on the momentum theory, a formulation was derived to represent slam load on a monopile. The slam load is approximated based on the impact area and impact velocity derived from the potential flow solver. As verified by the measurements, adding the slam load to waves which are identified as potential slamming, gives good approximation to the measurements. Taking the impact velocity for each slamming wave individually, results in a less conservative approximation of impact loads when compared to DNV guidelines. The developed method to identify and calculate slamming wave loads on monopiles structures can be further used in the evaluation of

turbine responses.

To conclude, the recommended practice is as follows:

- Wave train generation using OceanWave3D
- Identify potential slamming waves
- Apply added slam loading to Morison loads

## 6.2. Future work

Ideas for further developments, future work and possible subjects of interest are outlined below.

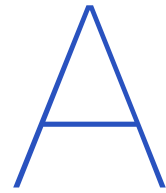
**Generate numerical sea state based on wave probe input files.** Although not available for this thesis, wave probe input files can be implemented in Oceanwave3D resulting in more accurate recreation of the measured sea state. This way the conclusions of this thesis can be further investigated and results verified.

**Validate identification method for slamming loads on sloping sea bed.** This thesis has focussed on breaking waves on a flat seabed. However, it could be of interest to compare the numerical identification method to breaking wave measurements on a sloping seabed. Hereby, the slamming wave analysis would be applicable to monopiles placed on sloping sea beds.

**Validate slam load formulation using computational fluid dynamics.** The current slam load representation is based on a 2-dimensional interpretation. A step further in validation would be using 3 Dimensional CFD to compare slam loads.

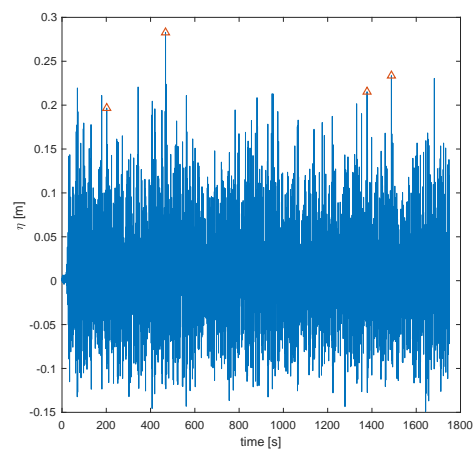
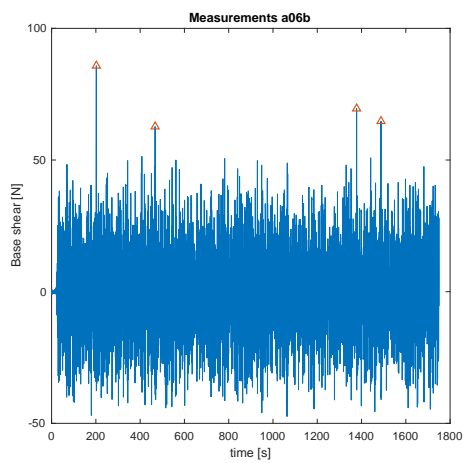
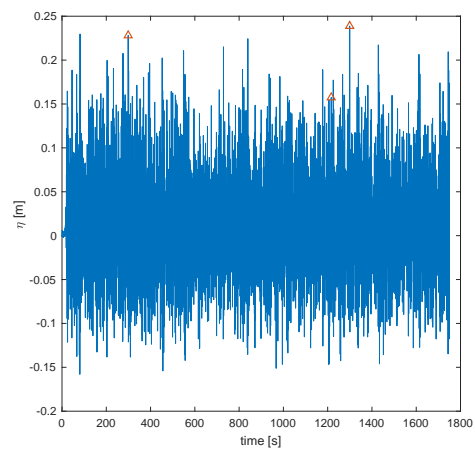
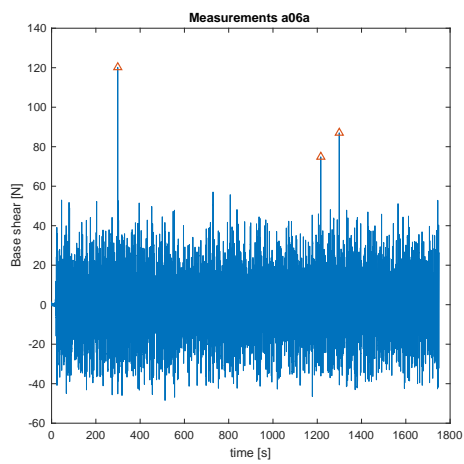
**Integrate slamming wave identification in Phatas and apply method for practical use.** In order to integrate the slamming wave identification method into Phatas, both the output from OceanWave3D and input for Phatas need to be aligned.

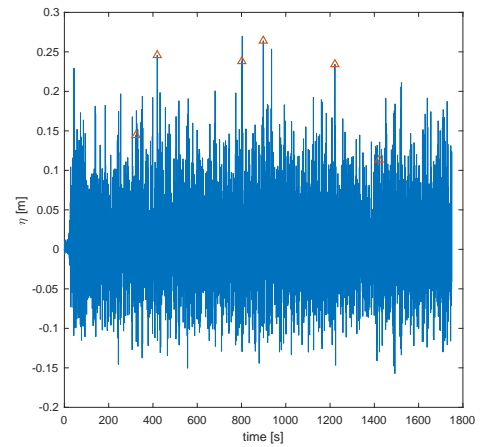
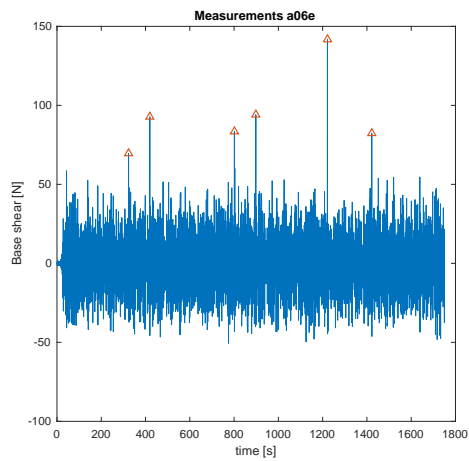
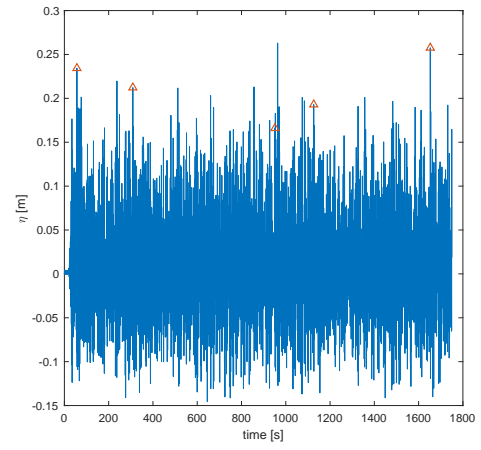
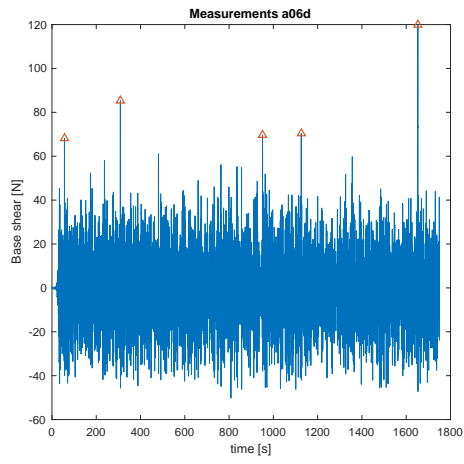
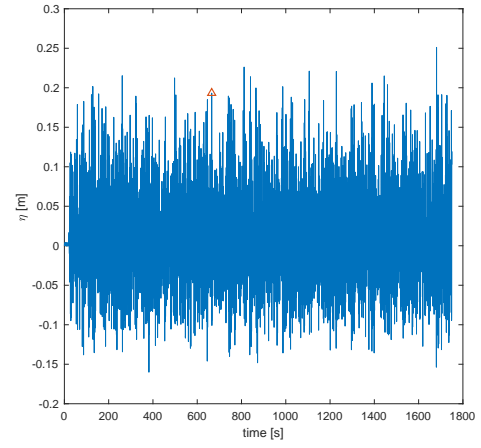
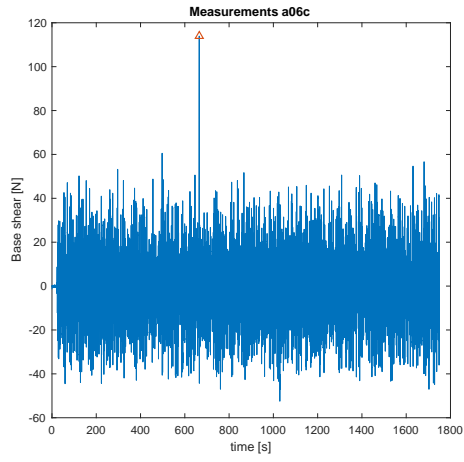




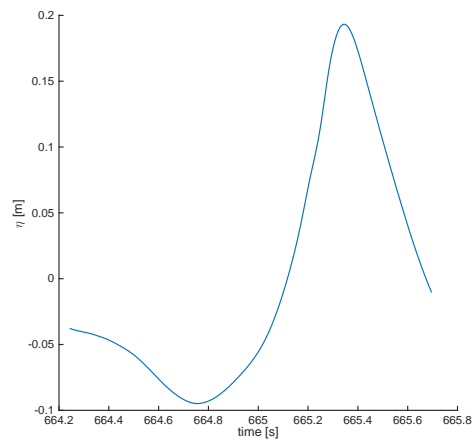
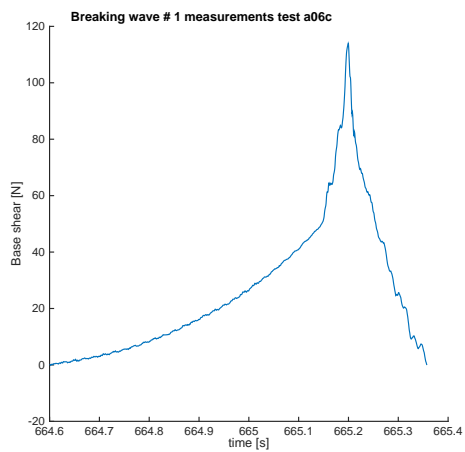
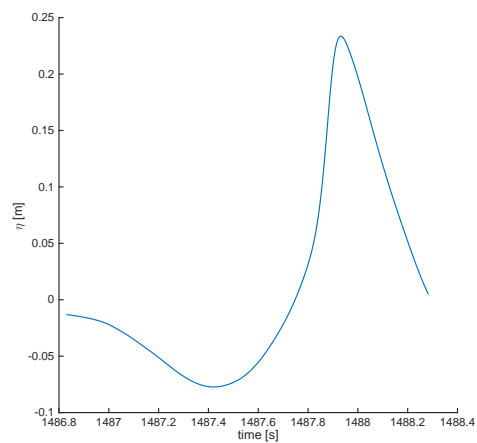
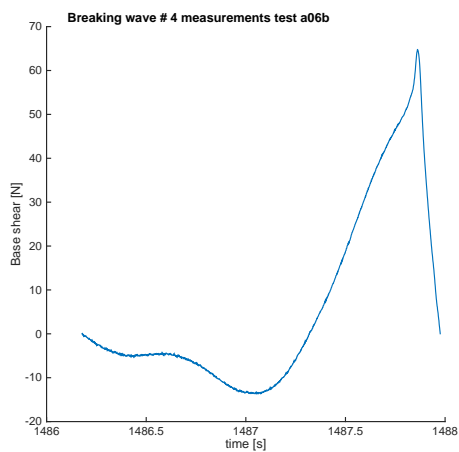
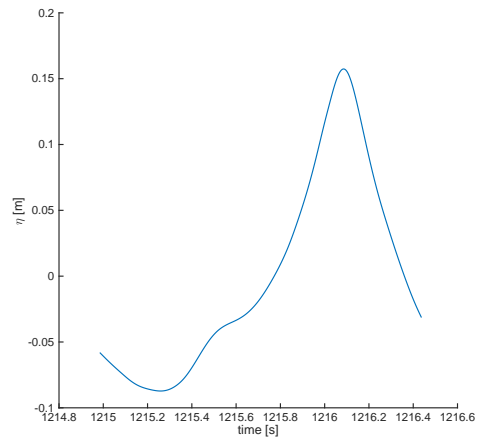
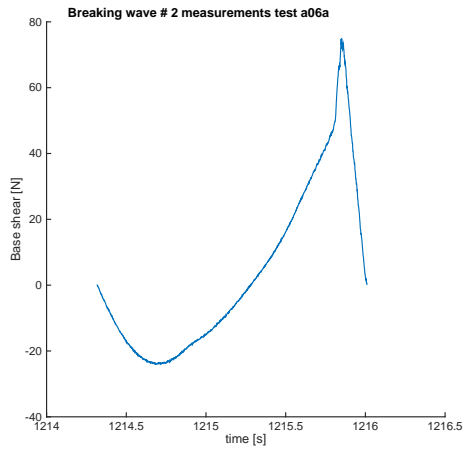
# Measurement data plots

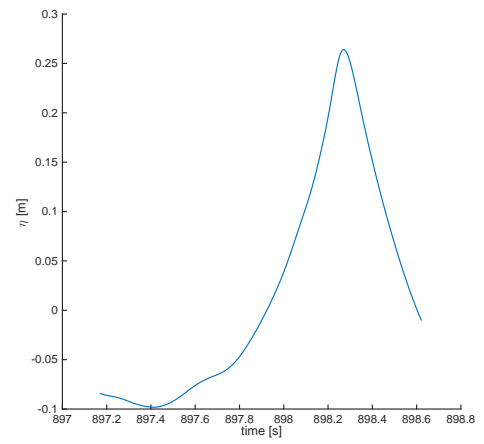
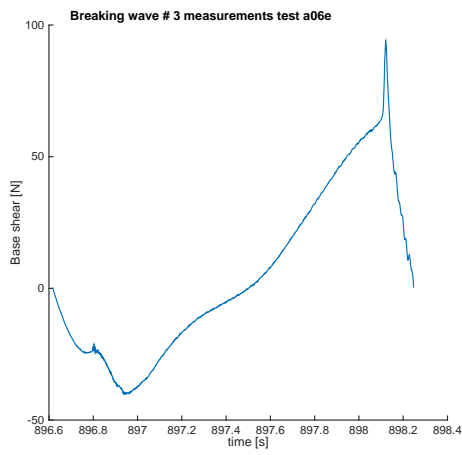
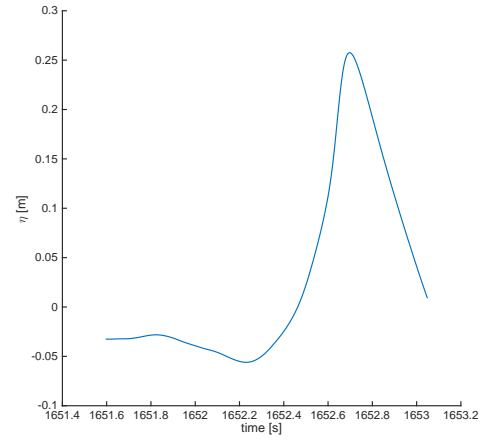
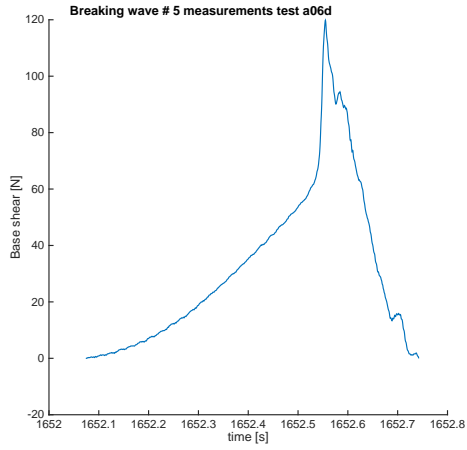
## A.1. Time series





## A.2. Individual waves

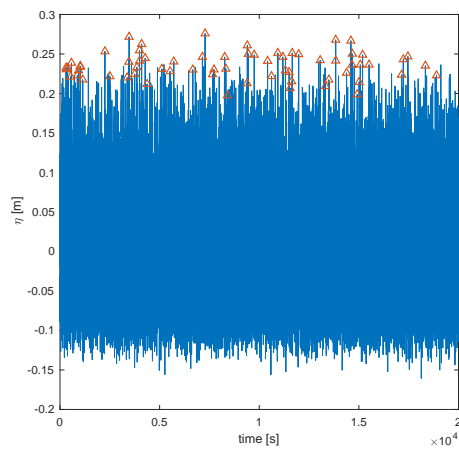
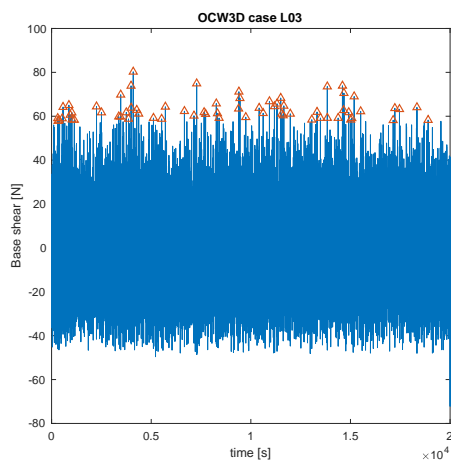




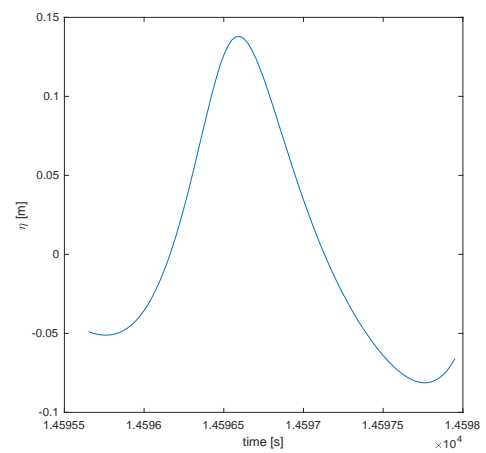
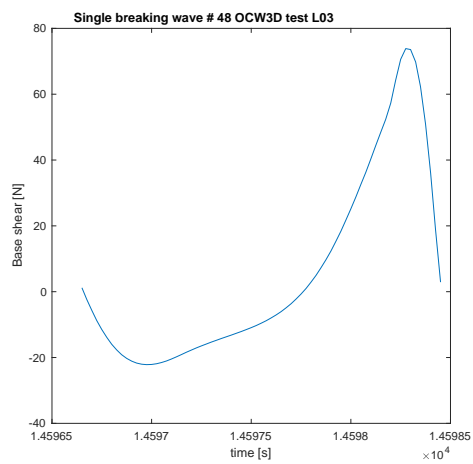
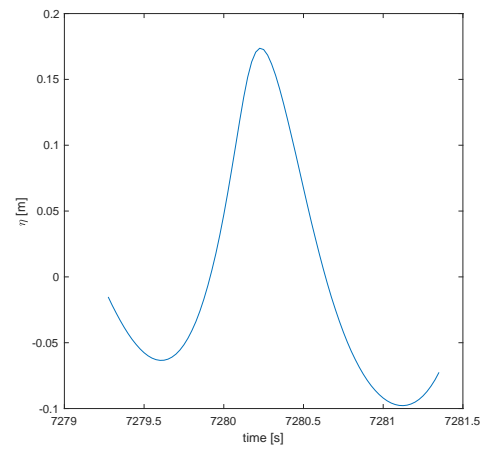
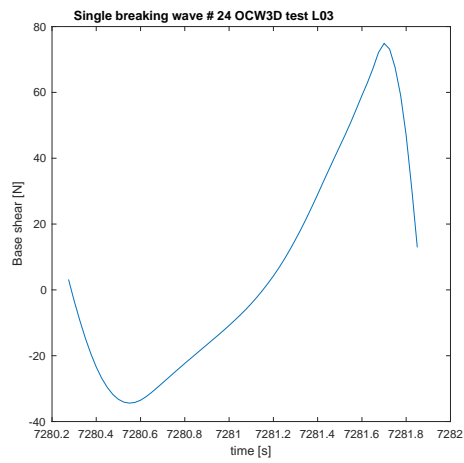
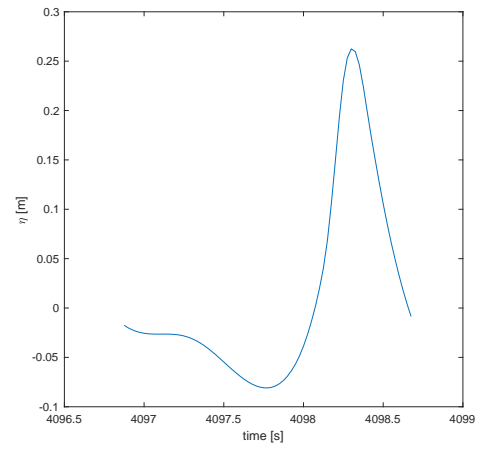
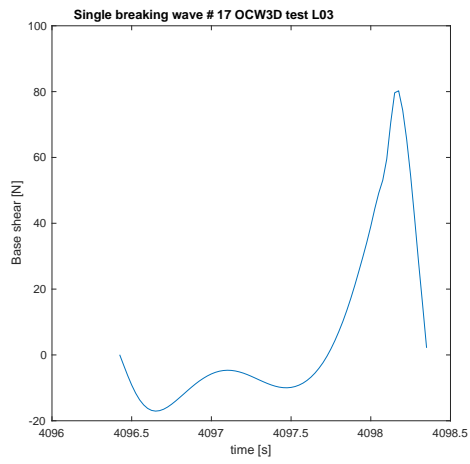
# B

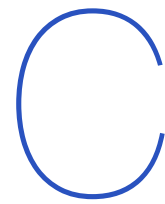
## OceanWave3D data plots

### B.1. Time series



### B.2. Individual wave plots





# OceanWave3D input

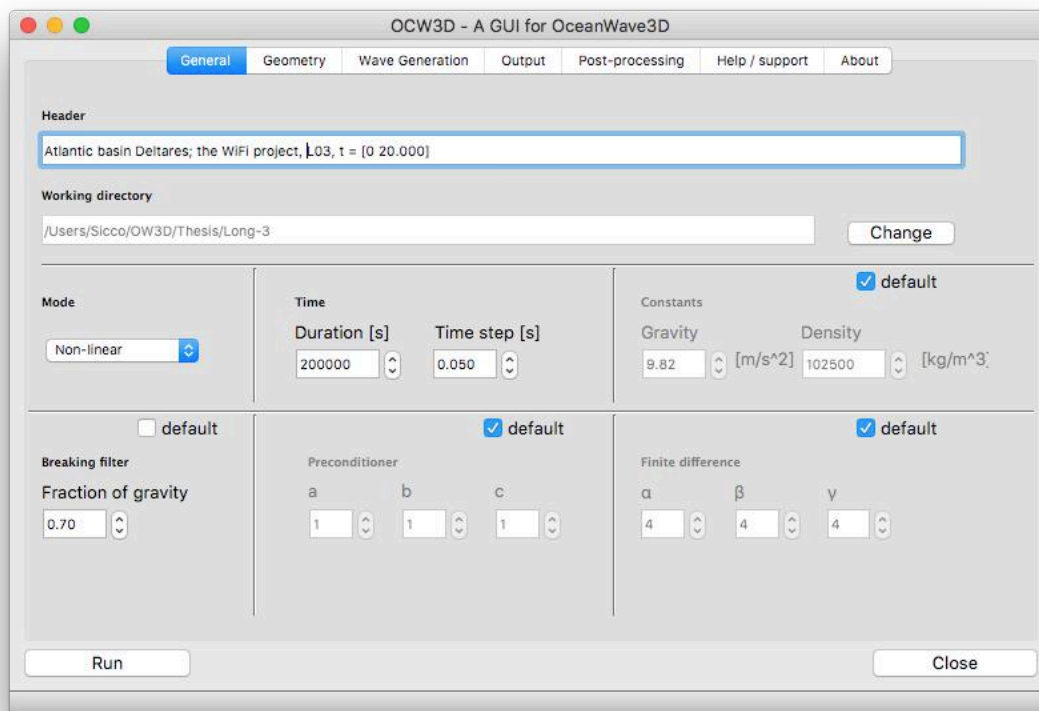
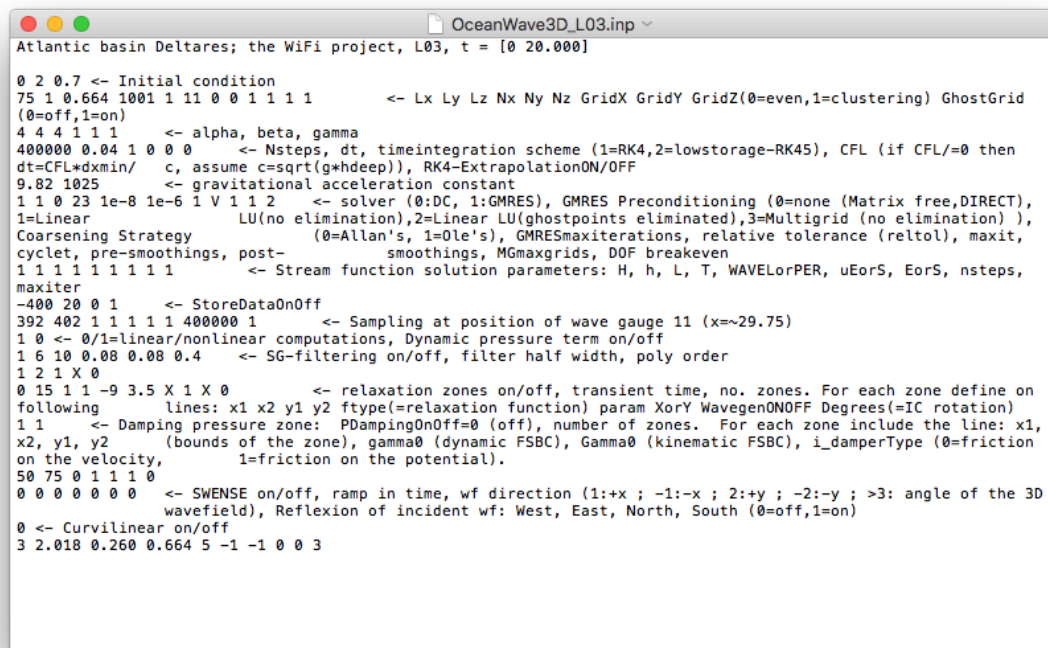


Figure C.1: Snapshot of GUI OCW3D to use OceanWave3D.



```

Atlantic basin Deltares; the WiFi project, L03, t = [0 20.000]

0 2 0.7 <- Initial condition
75 1 0.664 1001 1 11 0 0 1 1 1 1 <- Lx Ly Lz Nx Ny Nz GridX GridY GridZ(0=even,1=clustering) GhostGrid
(0=off,1=on)
4 4 4 1 1 1 <- alpha, beta, gamma
400000 0.04 1 0 0 0 <- Nsteps, dt, timeintegration scheme (1=RK4,2=lowstorage-RK45), CFL (if CFL/=0 then
dt=CFL*dxmin/ c, assume c=sqrt(g*hdeep)), RK4-ExtrapolationON/OFF
9.82 1025 <- gravitational acceleration constant
1 1 0 23 1e-8 1e-6 1 V 1 1 2 <- solver (0:DC, 1:GMRES), GMRES Preconditioning (0=none (Matrix free,DIRECT),
1=Linear LU(no elimination),2=Linear LU(ghostpoints eliminated),3=Multigrid (no elimination) ),
Coarsening Strategy (0=Allan's, 1=0le's), GMRESmaxiterations, relative tolerance (reltol), maxit,
cycllet, pre-smoothings, post-smoothings, MGmaxgrids, DOF breakeven
1 1 1 1 1 1 1 1 <- Stream function solution parameters: H, h, L, T, WAVElorPER, uEorS, EorS, nsteps,
maxiter
-400 20 0 1 <- StoreDataOnOff
392 402 1 1 1 1 1 400000 1 <- Sampling at position of wave gauge 11 (x~29.75)
1 0 <- 0/1=linear/nonlinear computations, Dynamic pressure term on/off
1 6 10 0.08 0.08 0.4 <- SG-filtering on/off, filter half width, poly order
1 2 1 X 0
0 15 1 1 -9 3.5 X 1 X 0 <- relaxation zones on/off, transient time, no. zones. For each zone define on
following lines: x1 x2 y1 y2 ftype(=relaxation function) param XorY WavegenONOFF Degrees(=IC rotation)
1 1 <- Damping pressure zone: PDampingOnOff=0 (off), number of zones. For each zone include the line: x1
x2, y1, y2 (bounds of the zone), gamma0 (dynamic FSBC), Gamma0 (kinematic FSBC), i_damperType (0=friction
on the velocity, 1=friction on the potential).
50 75 0 1 1 1 0
0 0 0 0 0 0 <- SWENSE on/off, ramp in time, wf direction (1:+x ; -1:-x ; 2:+y ; -2:-y ; >3: angle of the 3D
wavefield), Reflexion of incident wf: West, East, North, South (0=off,1=on)
0 <- Curvilinear on/off
3 2.018 0.260 0.664 5 -1 -1 0 0 3

```

Figure C.2: OceanWave3D input file.



# Bibliography

- [1] Battjes, J. Surf similarity, paper presented at 14th international conference on coastal engineering. *Am. Soc. of Civ. Eng., Copenhagen* (1974).
- [2] Brodtkorb, P., Johannesson, P., Lindgren, G., Rychlik, I., Rydén, J., and Sjö, E. WAFO - a Matlab toolbox for the analysis of random waves and loads. In *Proc. 10<sup>th</sup> Int. Offshore and Polar Eng. Conf., ISOPE, Seattle, USA* (2000), vol. 3, pp. 343–350.
- [3] Christensen, E. D., Bredmose, H., and Hansen, E. A. Extreme wave forces and wave run-up on offshore wind turbine foundations. *Proceedings of Copenhagen Offshore Wind* (2005), 1–10.
- [4] Dean, R. Stream function representation of nonlinear ocean waves. *Journal of Geophysical Research* 70, 18 (1965), 4561–4572.
- [5] DNV, G. Environmental conditions and environmental loads. *Recommend Practice DNV-RP-C205* (2014).
- [6] Engsig-Karup, A., Bingham, H., and Lindberg, O. An efficient flexible-order model for 3D nonlinear water waves. *Journal of Computational Physics* 228 (2009), 2100–2118.
- [7] European Commission. Paris agreement, 2015.
- [8] Faltinsen, O. Wave loads on offshore structures. *Annual review of fluid mechanics* 22, 1 (1990), 35–56.
- [9] Galvin, C. J. Breaker type classification on three laboratory beaches. *Journal of geophysical research* 73, 12 (1968), 3651–3659.
- [10] Holthuijsen, L. H. *Waves in oceanic and coastal waters*. Cambridge University Press, 2010.
- [11] Journée, J., and Massie, W. *Offshore hydromechanics*. TU Delft, 2000.
- [12] Longuet-Higgins, M. S. On wave breaking and the equilibrium spectrum of wind-generated waves. In *Proceedings of the Royal Society of London A: Mathematical, Physical and Engineering Sciences* (1969), vol. 310, The Royal Society, pp. 151–159.
- [13] Massel, S. R. *Ocean waves breaking and marine aerosol fluxes*, vol. 38. Springer Science & Business Media, 2007.

- [14] Morison, J., Johnson, J., Schaaf, S., et al. The force exerted by surface waves on piles. *Journal of Petroleum Technology* 2, 05 (1950), 149–154.
- [15] Paulsen, B., Bingham, H., and Bredmose, H. *Efficient computations of wave loads on offshore structures*. PhD thesis, 2013.
- [16] Paulsen, B. T., Bredmose, H., and Bingham, H. B. An efficient domain decomposition strategy for wave loads on surface piercing circular cylinders. *Coastal Engineering* 86 (2014), 57–76.
- [17] Paulsen, B. T., de Sonnevile, B., van der Meulen, M., and Jacobsen, N. G. Probability of wave slamming and the magnitude of slamming loads on offshore wind turbine foundations. - (2017).
- [18] Sarpkaya, T. Wave impact loads on cylinders.
- [19] SER. Energieakkoord voor duurzame groei, 2013.
- [20] Suja-Thauvin, L., Krokstad, J. R., Bachynski, E. E., and de Ridder, E.-J. Experimental results of a multimode monopile offshore wind turbine support structure subjected to steep and breaking irregular waves. *Ocean Engineering* 146 (2017), 339–351.
- [21] Wienke, J., Sparboom, U., and Oumeraci, H. Breaking wave impact on a slender cylinder. In *Coastal Engineering 2000*. 2001, pp. 1787–1798.
- [22] Williams, J. Limiting gravity waves in water of finite depth. *Philosophical Transactions of the Royal Society of London A: Mathematical, Physical and Engineering Sciences* 302, 1466 (1981), 139–188.